J. Fluid Mech. (2025), *vol.* 1025, A7, doi:10.1017/jfm.2025.10924

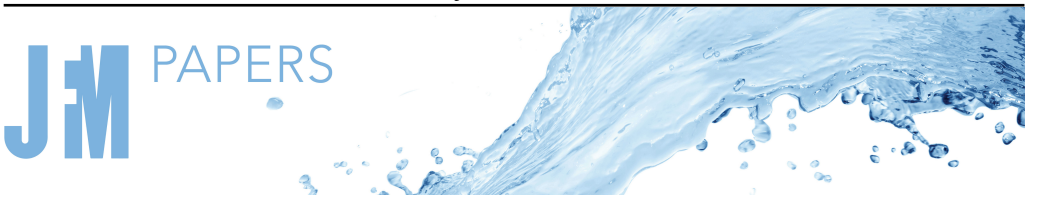

Spray behaviour from non-swirling to swirling gas jet in coaxial atomisation

Santanu Kumar Sahoo[1], **Yu Wei**[1] **and Nathanaël Machicoane**[1]

[1]Univ. Grenoble Alpes, CNRS, Grenoble INP, LEGI, 38000 Grenoble, France

Corresponding authors: Santanu Kumar Sahoo, santanuksahoo1@gmail.com; Nathanaël Machicoane, nathanael.machicoane@univ-grenoble-alpes.fr

(Received 25 February 2025; revised 31 October 2025; accepted 3 November 2025)

The present study focuses on the influence of gas swirl on the spray behaviour from a two-fluid coaxial atomiser with high gas-to-liquid dynamic pressure ratios M by varying both the liquid Reynolds number Re_l and the gas Weber number We_g. The investigations identify the deviations of the carrier phase velocity fields, droplet distribution, and dispersion when swirl is introduced to the gas phase compared with the non-swirling conditions. The changes in the axial, radial and tangential velocities of the continuous phase due to the introduction of swirl are highlighted while retaining a self-similar behaviour. The slip velocity of the large droplets in swirling sprays is negative, unlike the known positive value for non-swirling sprays. The shape of the radial profiles of the mean drop size is investigated along We_g, notably revealing an inflection point for swirling sprays at high-We_g values. A global assessment of the drop size uncovered that swirl leads to its increase for low M while assisting spray formation at high M. Additionally, the radial profiles of axial fluxes for swirling sprays have a wider bell-shaped curve compared with non-swirling sprays at high M, unlike the off-centre maxima found for low M. However, the mentioned dependencies of drop sizes and fluxes cannot be determined by M solely for intermediate gas-to-liquid momentum ratios ($23 < M < 46$), and vary with Re_l and We_g. In addition, the response of at least the mean droplets at the edge of the spray to the large gas eddies shows a linear relation with swirl intensity.

Key words: multiphase flow, gas/liquid flow

1. Introduction

Sprays, a collection of polydisperse droplets, have wide applications at various scales that include fuel spray production for combustion in different engines (Hardalupas, Taylor & Whitelaw 1990; Singh *et al.* 2020), targeted drug delivery in biological flows (Gürzing *et al.* 2022), metal powder production for additive manufacturing (Ünal 1989; Qaddah *et al.* 2024), cleaning in the semiconductor industry (Lallart *et al.* 2024), agricultural

sprays (Makhnenko *et al.* 2021), cooling for various applications such as data centres (Kandasamy *et al.* 2022) and coating of surfaces such as in the pharmaceutical industry (Muliadi & Sojka 2010). The recent investigations span towards real-time feedback control of the spray features (Osuna-Orozco *et al.* 2019, 2020, 2022). Bulk liquid is fragmented to form droplets with tailored characteristic sizes, distributions and associated velocities tailored for these applications. One of the commonly used methods relies on high-pressure liquid ejection, resulting in shear-driven hydrodynamic instability of high-velocity bulk liquid to form droplets. In most practical applications, this method is accompanied by an assisted air stream that further enhances the instabilities and leads to an augmented droplet formation process (Dumouchel 2008). In such cases, the fundamental mechanism driving the enhanced break up of the bulk liquid is an increase in stresses (Lasheras & Hopfinger 2000). With a view to further contribute to the existing stresses for droplet generation and modify the dispersion, an accompanied tangential component can be employed by the introduction of swirling motion to the gas jet (Hardalupas & Whitelaw 1994; Hopfinger & Lasheras 1996). We investigate such a configuration here.

In single phase already, the high-momentum round jet has rich dynamics. Some of the key features include near orifice Kelvin–Helmholtz (K-H) instabilities (Crow & Champagne 1971), a potential core (Ko & Davies 1971), a universal spread-rate of ≈ 0.1 (Panchapakesan & Lumley 1993; Pope 2001), self-similar velocity behaviour (Hussein, Capp & George 1994), entrainment (Liepmann & Gharib 1992) and helical modes away from the nozzle (Takahashi *et al.* 2023). Furthermore, the outer shear layer formed from the jet constitutes growing vortices whose convection velocity is given by (Dimotakis, Miake-Lye & Papantoniou 1983)

$$U_c = \frac{\sqrt{\rho_1}U_1 + \sqrt{\rho_2}U_2}{\sqrt{\rho_1} + \sqrt{\rho_2}}, \tag{1.1}$$

where 1 and 2 represent two different fluid streams, here the fluid of the jet and the fluid into which the jet is discharged. ρ and U represent the density and velocity of the fluid streams, respectively. A similar behaviour is observed in the case of annular jets (Kuhlman 1987). In coaxial atomisers, a central round liquid jet is surrounded by an annular gas jet, which are typically low and high momentum, respectively. Many of the gas jet features get altered due to the low momentum liquid at the centre, and along with their transport, affect the spray generation process, the gas-phase velocity, the droplet dynamics and dispersion (Rehab, Villermaux & Hopfinger 1997; Favre-Marinet, Camano & Sarboch 1999). Therefore, a coherent comparison in the gas-jet Reynolds number of industrial relevance can be instrumental in characterising the spray. In addition, when the gas swirl intensity is high, vortex breakdown is observed near the injector due to low pressure at the centre of the jet (Billant, Chomaz & Huerre 1998), yet another feature that needs to be considered when investigating the spray in the presence of a swirling gas configuration (Rajamanickam & Basu 2017). This high swirling flow essentially includes the presence of a stagnation point due to its imposition of adverse pressure gradient in the gas flow, resulting in a recirculation zone with a central core (Oberleithner *et al.* 2011; Rajamanickam & Basu 2018).

Investigations on the influence of gas swirl on sprays have spanned many flow configurations. For example, Ade *et al.* (2023) investigated the influence of swirling gas on the breakup of a single droplet and found that, under high swirling conditions, finer satellite droplets are formed. Such an influence of the swirl is also observed by Rostami, Li & Kheirkhah (2025) for droplets with a wide range of velocities in a spray from a pressure-swirl atomiser introduced into a swirling coflow. In addition, Rostami, Li & Kheirkhah (2024) addressed the influence of coflowing swirling air on large-Stokes-number sprays and showed that swirl affects the important length scales of clusters,

the number density of droplets in those clusters, and the most probable drop size in different clusters. In coaxial atomisation, in addition to such droplet and swirled-flow interactions, the angular momentum imparted to the gas jet plays a role in the spray formation mechanisms, as well as in the droplet dispersion and breakup/coalescence balance farther downstream.

The spray formation mechanism in a coaxial atomiser entails a sequence of processes (Lasheras & Hopfinger 2000). As the liquid and gas phases come in contact near the atomiser, the shear instability is developed and leads to the formation of interfacial waves on the liquid jet (Marmottant & Villermaux 2004; Matas, Delon & Cartellier 2018). At low gas momentum conditions, the asymmetric nature of these waves with gradual downstream progression leads to the flapping instability where the jet meanders radially (Delon, Cartellier & Matas 2018). The liquid jet's shape formed by the flapping instability promotes the formation of membranes, where the liquid is first flattened, then inflated into a bag with a thin film and a thicker rim, a regime of shear breakup referred to as bag breakup. With supporting numerical (Zandian, Sirignano & Hussain 2018; Ling *et al.* 2019) and experimental (Lozano & Barreras 2001; Delon *et al.* 2018) investigations, it is established that the flapping of the liquid jet is due to the formation of local recirculation zones in the wake of the jet, leading to alternating low-pressure and high-pressure zones. Alternatively, at high We_g, the interfacial perturbations stretch to form ligaments that detach from the bulk liquid or may form droplets due to Rayleigh–Taylor instability with minimal large-scale movement (Lasheras & Hopfinger 2000), in what is called fibre-type atomisation. The resultant morphology and the flow field resemble a backward-facing step where the fine droplets are at the edge, and the big ones are at the centre (Huck *et al.* 2022). While the potential modifications of the nature of the instabilities of the liquid jet by swirl addition to the gas jet received little attention, their magnitudes and frequencies are observed to vary (Kumar & Sahu 2019; Machicoane *et al.* 2020).

In coaxial atomisation, the central core in swirling gas flows makes the bulk liquid expand while breaking up (Hopfinger & Lasheras 1996; Dunand, Carreau & Roger 2005). As a result, although an apparent change in the spray evolution is observed by Préaux *et al.* (1998), it has not been explored in depth unlike the well-characterised non-swirling counterpart. For straight gas jets, it is reported that vortices generated by the K-H waves can influence the trajectory of droplets following their breakup. For example, in planar shear layers, the recirculation region formed downstream of these waves catapult the droplets to eject them at very high angles compared with the primary momentum direction (Jerome *et al.* 2013). Such high-angle ejections are also mentioned in coaxial atomisation by Huck *et al.* (2022). While these observations are limited to low gas momentum conditions, at high momentum, other factors such as high-entrainment rates, the substantial dominance of the helical modes associated with the gas jet without or with swirl also plays a key role in the organisation of the droplets (Dunand *et al.* 2005). Such features happen in parallel to the expected reduction in the spray drop size as the gas momentum (and kinetic energy) increases. This effect also comes with a reduction in the spray cone angle. Therefore, additional methods like swirl hold immense relevance, since gas swirl can mitigate or counteract the reduction in the spray dispersion.

Sustained high gas momentum following the breakup of droplets (as a very small fraction of the kinetic energy is contributing the formation of droplets (Yarin, Roisman & Tropea 2017)) will drive the transport for the majority of the droplets. For the big droplets, though, which contribute significantly to the volumetric quantities such as mass flux, the response to the gas flow is more complicated. Such flow investigations have close allegiance with the works on particle-laden jets (PLJs) due to the retaining of the droplet size far from the developing region and their sparse concentration in the carrier fluid.

Undoubtedly this comparison does not apply to either the near-field breakup and the dense concentration region dynamics in particle-laden flows mentioned in the regime map of Brandt & Coletti (2022). The most important parameter for investigating these flows identifies the response of particles or droplets, ascertained by the ratio of their response time scale (τ_p) with respect to the carrier flow time scales (τ_f) called the Stokes number (Squires & Eaton 1990):

$$St = \tau_p/\tau_f. \tag{1.2}$$

The general consensus in this regard is that particles perfectly follow the flow when $St < 0.01$, and do not respond when this value is greater than 10 (Balachandar & Eaton 2010). Particles with $0.01 < St < 10$ are known to respond to the flow partially. Earlier investigations by Modarress, Tan & Elghobashi 1984; Hardalupas, Taylor & Whitelaw 1989) examined these aspects and identified the mechanisms for energy transfer between the dispersed and the continuous phase. With a similar theme, the investigations by Longmire & Eaton (1992), Lazaro & Lasheras (1992) investigated a shear layer with particles and reported about particle dispersion for $St = 1$. Apart from the significant focus on the clustering behaviour of particles and droplets (Sahu *et al.* 2018; Manish & Sahu 2019; Angriman *et al.* 2022), which is a consequence of the interaction of carrier phase eddies with the droplets, additional factors determining the particles' response to flow have been brought forward by recent investigations of Lau & Nathan (2014,2016). This includes linking the initial conditions to the reduced dispersion of particles with increasing Stokes number in the far field of the PLJs. This analysis pointed to an interesting competition between the Saffman force acting on the high-Stokes-number particles to bring them to the centreline and turbophoresis acting on particles with small St to accumulate them near the edges when investigating dispersion near the exit of the jet. The investigations on dispersion presented earlier by Hardalupas & Whitelaw (1994), recently by Huck *et al.* (2022) for non-swirling sprays and more recently by Fong *et al.* (2024) for swirling sprays unify the commonalities but are far from exhaustive to fully understand the dispersion of droplets in sprays, especially in the presence of gas swirl.

Numerous investigations over many decades have focused significantly on the instabilities in the liquid jet leading to its breakup (Marmottant & Villermaux 2004; Matas *et al.* 2018; Kumar & Sahu 2019). Despite the realisation that the downstream evolution of droplets cannot be easily related to the upstream breakup regimes, there are very few assessments for the former. To make these investigations relevant, diverse fluid dynamic quantities must be determined. For example, it is essential from the perspective of applications to understand the gas flow properties that can influence momentum transport. In reacting systems, the carrier phase also determines energy transfer (Gounder, Kourmatzis & Masri 2012). For such analyses, there is a scarce presence of investigations with physically relevant quantities in the context of sprays. With increased realisation of the benefits of swirling environment in combustion applications (Hoffmann, Lenze & Eickhoff 1997; Kwark *et al.* 2005) and metal powder production (Qaddah *et al.* 2024), it is pertinent to make such investigations for swirling sprays. Although recent advancements in this regard have shed new light, the applicability is limited to only a narrow parameter range. These considerations severely undermine the significant differences in the breakup behaviour near the atomiser and the existing understanding of their relation as the droplets travel downstream. Additionally, the response of large droplets in the carrier phase, which can be instrumental in applying the understanding of the PLJs for modelling, is almost negligible in the literature in the case of swirling sprays.

Therefore, the present investigation addresses these gaps in the literature on swirling sprays. The experimental details are described in § 2. An overview of the spray generation

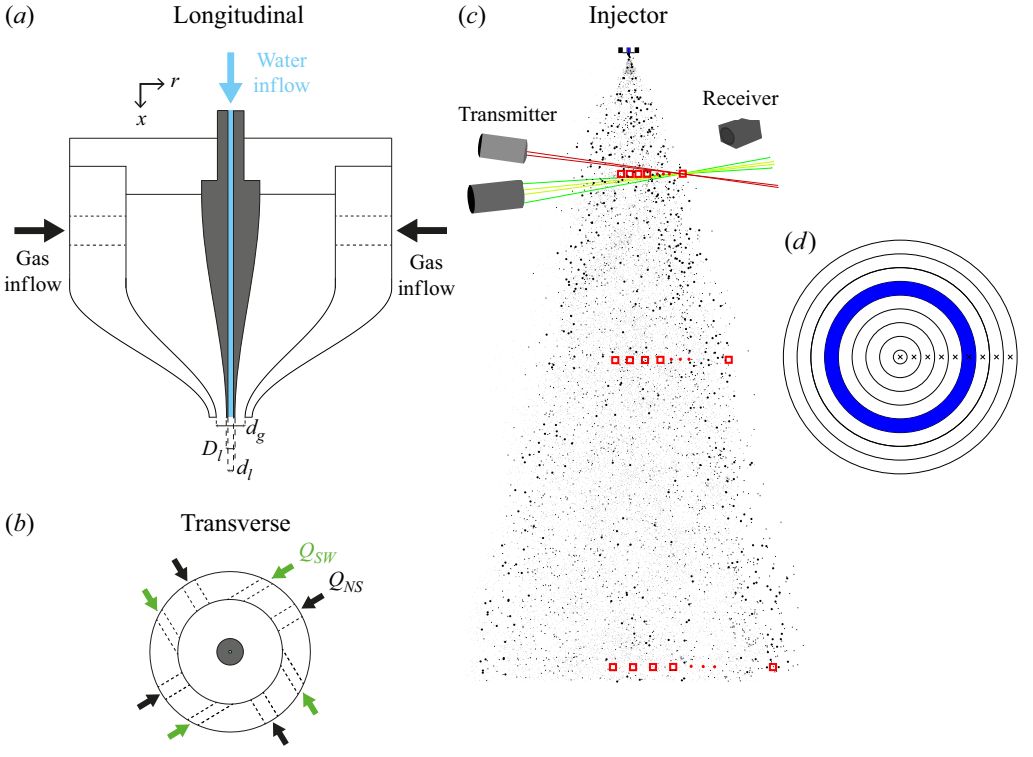

Figure 1. Spray generation configuration and measurement technique. Coaxial atomiser used in the present experiments in a longitudinal cut (a), and (b) a cross-section in the plane of the gas inlets. (c) The PDPA arrangement and measurement locations in a spray longitudinal view and (d) cross-sectional view, with anuli of area S_i representing each measurement location i.

mechanisms is provided in § 3. We follow it up with the investigations of the kinematics of the swirling flow in § 4. A comprehensive droplet size analysis is presented in § 5, which is followed by the results on spray dispersion in § 6. We close the findings of this article with a discussion and conclusion (§ 7).

2. Experimental details

A two-fluid atomiser (shown in figure 1a), where a central liquid jet is injected coaxially along with an annular gas jet, is used here to generate the spray. The atomisation process is initiated when the liquid jet comes in contact with the turbulent gas. In the atomiser, the central liquid jet with exit diameter d_l, resulting in the exit area $A_l = \pi d_l^2/4$, is fully developed, and controlled by the volume flow rate of Q_l. Subscripts l and g represent the liquid and gas-phase parameters, respectively. The liquid exit velocity and Reynolds number are calculated as $U_l = Q_l/A_l$ and $Re_l = U_l d_l/\nu_l$, respectively, where ν_l is the kinematic viscosity of liquid.

For the gas flow, there are two sets of inlets. One set of four inlets, intended for axial gas stream at the exit, is through four streams impinging onto the atomiser axis, with a cumulative volume flow rate of Q_{NS}. On the other hand, tangential motion to the gas flow is imparted through the second set of four inlets, which are directed into the atomiser off-axis as shown in figure 1(b), with a cumulative volume flow rate of Q_{SW}. These two sets of inlets combine in the gas nozzle to provide the total volume flow rate of gas,

Case	U_l (m s^{-1})	Re_l	U_g (m s^{-1})	Re_g	We_g	M	m	SR
1	0.6	1120	82	52 000	210	23	0.24	0, 0.8
2	0.6	1120	115	72 700	420	46	0.17	0, 0.8
3	0.6	1120	163	102 400	830	90	0.12	0 : 0.2 : 1
4	0.6	1120	203	127 700	1280	140	0.1	0, 0.8
5	1.2	2230	163	102 400	830	23	0.24	0, 0.8
6	2.3	4350	163	102 400	830	6	0.47	0, 0.8
7	4.5	8480	163	102 400	830	2	0.91	0, 0.8

Table 1. The table of conditions for characterising swirling sprays, reporting the associated liquid Reynolds number $Re_l = U_l d_l/\nu_l$, gas Reynolds number $Re_g = (U_g\sqrt{4A_g/\pi})/\nu_g$ and Weber number $We_g = \rho_g U_g^2 d_l/\sigma$, gas-to-liquid dynamic pressure ratio $M = \rho_g U_g^2/\rho_l U_l^2$, liquid mass loading $m = \rho_l A_l U_l/\rho_g A_g U_g$ and swirl ratio $SR = Q_{SW}/Q_{NS}$. The axial location where measurements take place is $x/d_g = 25$ for all conditions. In addition, for case 3 with $SR = 0$ and 0.8, the spray is investigated at $x/d_g = 10$ and 50. At each measured axial distance, at least a dozen radial locations are probed.

$Q_g = Q_{NS} + Q_{SW}$. The acquired swirl in the gas flow is characterised by the swirl ratio, $SR = Q_{NS}/Q_{SW}$. The annular exit of the nozzle has inner and outer diameters as D_l and d_g, resulting in the gas exit area, $A_g = \pi(d_g^2 - D_l^2)/4$. The gas exit velocity (U_g), Reynolds number (Re_g) and Weber number (We_g) are calculated as Q_g/A_g, $(4U_g\sqrt{4A_g/\pi})/\nu_g$ and $\rho_g U_g^2 d_l/\sigma$, respectively, where ν_g is the kinematic viscosity, ρ_g is the density of the gas and σ is the surface tension of the liquid and gas interface. In addition to parameterising the liquid and gas flow separately, they are combined through the gas-to-liquid dynamic pressure $M = \rho_g U_g^2/(\rho_l U_l^2)$ and liquid mass loading number $m = \rho_l A_l U_l/(\rho_g A_g U_g)$, where ρ_l is the density of the liquid.

In the present experiments, distilled water is used for liquid and filtered compressed air for the gas phase. Note that all the physical properties of water and air are considered at 20 °C, which was the average room temperature while conducting the experiments and less than 1.5 °C variation was noted around this average. The experimental facility is a recurring one as used in Tolfts *et al.* (2023, 2024) and has been characterised well in proximity to the operating range in the present study. A proportional–integral–derivative (PID) controller is used to keep the liquid and gas flow rates constant over the measurement period. They are measured along with droplet measurements so that the actual measured average flow rate (and not set values) are used to compute non-dimensional groups. In addition, this variation over the measurement duration (up to 25 minutes) was always less than 2 % over all conditions. The flow conditions for the present experiment are given in table 1.

The measurements of the resulting drops after atomisation are performed using a phase Doppler particle analyser (PDPA) as shown in figure 1(*c*,*d*). The PDPA is configured in a forward scattering mode with the scattering signal receiving angle (θ) of 49° for measuring droplet size (d), axial (u_x), radial (u_r) and tangential (u_θ) velocities in a coincident mode. The size and velocity measurements are considered point-wise and the measurement system is raster-scanned at different radial locations. The droplets were phase-validated to ensure accuracy in the measurements. The collimating lens ($f_c = 500$ mm) and the imaging lens ($f_i = 500$ mm) were used with a constant magnification ($\beta = -f_i/f_c$). The pairs of laser beams corresponding to u_x and u_r intersect to form a prolate spheroid. The probe for the third pair intended to compute u_θ is at 30° with respect to the other transmitter and intersects at the exact location (aligned to cross the probe volume with

a pinhole of 50 μm). The length of this probe volume is truncated using the spatial filter whose slit width is $s = 200$ μm. Together with the receiving probe angle and the magnification, the effective length of the cylindrical probe volume is $s/|\beta|\sin\theta$. With a motive to find the cylindrical cross-section of the probe volume, which is dependent on the size of droplets due to the Gaussian nature of the laser beam, we find the product of the axial velocity of the droplets and the residence time to find the size-dependent path length l (Albrecht *et al.* 2003). A fit to determine the relation of l with binned diameters of droplets was applied during the post-processing of the data. Using all the configuration values, we find the probe's cross-sectional area,

$$\mathcal{A} = \frac{\ell s \cos\gamma}{|\beta| \sin\theta}, \tag{2.1}$$

and the probe volume,

$$\mathcal{V} = \frac{\pi}{4} \frac{\ell^2 s \cos\gamma}{|\beta| \sin\theta}, \tag{2.2}$$

where γ is the angle subtended by u_x with u_r.

In the present measurements, the drop size is in the range of $d = 1-100$ μm. This size range is considered to accurately characterise the surrounding gas phase in the spray, conditioning for the small droplets, and also to measure a significant proportion of the droplet population. From the small droplets, we determine the Stokes number *a posteriori* based on the exit conditions of the nozzle, given by

$$St_d = \frac{\tau_p}{d_g/U_g}, \tag{2.3}$$

where $\tau_p = \rho_\ell d^2/(18\rho_g \nu_g)$ is the droplet response time scale. This Stokes number (St_d) is calculated for droplets of different sizes d. We observe that for $d < 5$ μm, St_d for different gas Reynolds numbers under investigation is always less than 0.002. With the increase in the downstream distance of the droplets, the Stokes number also decreases quickly as the flow time scale $\propto x^2$ in a PLJ flow (Hardalupas *et al.* 1989). Such droplets were therefore assumed to be the tracer particles of the gas phase.

Due to the choice of range that does not capture the entirety of the droplet population for a few locations and conditions, we will only discuss the probability density function (since although 'clipped' they are not biased by that) and arithmetic mean diameter, given by $d_{nm} = \Sigma_i N_i d_i^n / \Sigma N_i d_i^m$ with $n = 1$ and $m = 0$, where N represents the number of drops corresponding to each drop size bin d_i. The arithmetic mean diameter in most cases here correspond to the most probable droplet size. We refrain from analysing other diameters such as d_{20} or d_{32} to avoid truncated calculations of the contribution from bigger droplets.

In addition, we characterise the gas phase in the absence of the spray and for non-swirling conditions using a single probe hotwire anemometer. The measurements are acquired at a sampling rate of 20 kHz for 10 s at each location. As a straight gas jet is known to have the radial velocity u_r one order of magnitude less than the axial velocity u_x (Pope 2001), this measurement was considered robust enough to understand the axial flow characteristics with minimal bias.

3. Spray formation mechanisms

The spray development from the near atomiser to the far field is presented in figure 2 (supplementary movies corresponding to these conditions are available at https://doi.org/10.1017/jfm.2025.10924). The left half of the image in each panel is the

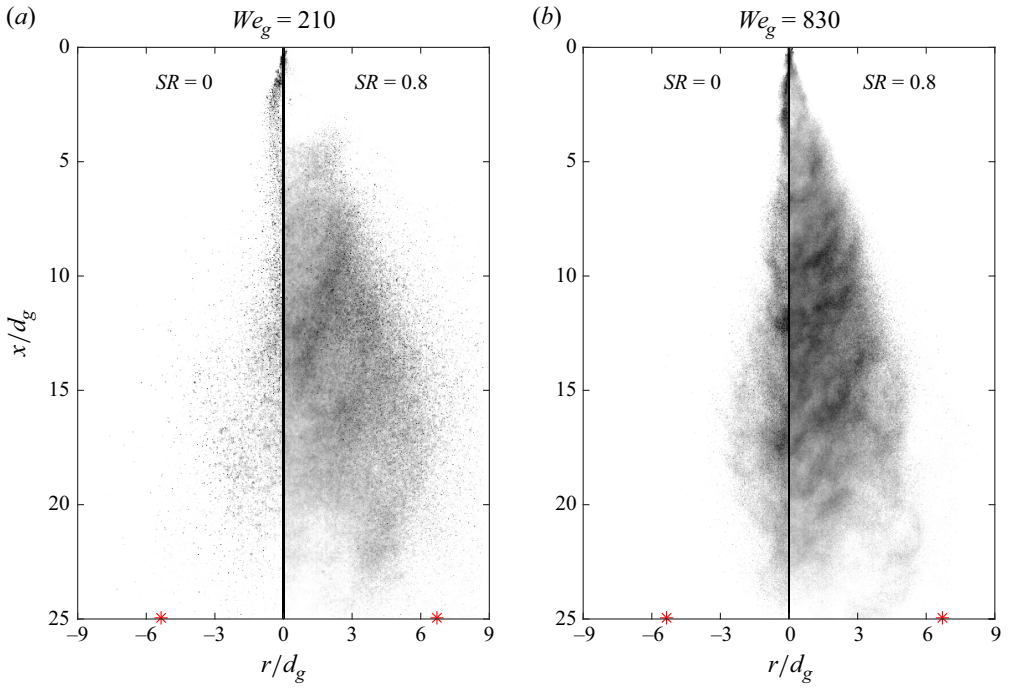

Figure 2. Spray scattering images showing the global spray features at $SR = 0$ (left half of the image in each panel) and $SR = 0.8$ (right half of the image in each panel) with their respective adius at 10 % centerline velocity, $r_{0.1}$ locations given in red marks at $x/d_g = 25$ for $Re_l = 1120$ and (*a*) $We_g = 210$, (*b*) $We_g = 830$. The spatial inhomogeneities, especially visible in (*a*), are a direct signature of the flapping instability.

non-swirling condition ($SR = 0$), and the right half is the swirling condition ($SR = 0.8$). Very evident from the instantaneous snapshots is the large-scale flapping motion of the liquid jet at low M (figure 2*a*) due to which the non-swirling spray near the atomiser is seen tilted to the left side. In contrast, the swirling jet is not visible very close to the atomiser, being tilted to the opposite side in figure 2(*b*). The supplementary movies reveal a high degree of flapping in the case of swirling sprays compared with their non-swirling conditions, qualitatively confirming that the increased flapping amplitude reported at low We_g by Kaczmarek *et al.* (2022) also occurs at higher gas Weber numbers. The consequent spatially varying spray structure is distinct, which appears to be less dense for $SR = 0$ than for $SR = 0.8$, the scattering signal being less pronounced indicating that the swirling cases produce a higher number of smaller droplets here. The red marks at $x/d_g = 25$ indicate the location where $u_{x,0}$ equals the mean centreline velocity of the gas jet, $u_{0.1}(x, r_{0.1}) = u_x(x, r = 0)/10$. An imaginary line (not drawn here as a measurement of the virtual origin is lacking here) joining the atomiser exit and the $r_{0.1}$ location indicates an increase in the angle of the swirling gas jet compared with a non-swirling one. In addition, numerous large droplets eject beyond this limit at various axial distances at low M for both $SR = 0$ and 0.8. The observation for $SR = 0$ matches with the findings of Huck *et al.* (2022).

Different from this behaviour, at high M, the spray is less affected by the flapping instability (which occurs at higher frequency, and over a smaller amplitude) near the atomiser (figure 2*b*) with the presence of spatially varying intermediate and high drop density regions farther away. This may be considered as a visual indication of the larger role played by turbulent fluctuations in sprays at higher M. A keen observation of the

$r_{0.1}$ locations indicates two important features at high M: (i) while for $SR = 0$ almost all the droplets are within an imaginary line joining the atomiser exit and the $r_{0.1}$ (similar observation as of Huck *et al.* 2022), droplets go beyond this line for the swirling spray, (ii) the $r_{0.1}$ location almost remains unchanged in comparison with low M at fixed SR, indicating that the spreading is not affected much due to change in We_g if the swirl ratio is constant.

A few important questions that arise for better understanding the resultant spray of figure 2 are how the droplet velocity varies with different parameters, what is the consequent droplet distribution, and how does spray dispersion behaviour vary with governing parameters. Longmire & Eaton (1992) reported that, in the case of PLJs, large-scale eddies of the gas jet contribute to the transport of particles. Moreover, in the case of swirling jets, in addition to the helical structures, three-dimensional motions are imposed. In light of this fact, although there is a higher tangential flux of the gas at higher We_g for the same swirl value, it does not lead to more spread of the droplets. Therefore, in the next section, we investigate the carrier phase to determine the counter-intuitive nature of the spread of droplets.

4. Kinematics

We remind the reader here that the measurement of the gas jet is conducted using hotwire anemometry in the absence of spray and using the small droplets in its presence. For a more detailed explanation of the methodology, the reader is referred to § 2. From these measurements, we investigate the first-order statistics of all the velocity components of the gas to characterise the carrier phase in the presence of spray.

4.1. *Mean axial velocity (u_x)*

The behaviour of the axial velocity of the turbulent annular gas jet is shown in figure 3. Figure 3(*a*) presents the radial profiles of the mean axial velocity (u_x). Lines and markers represent the hotwire and PDPA data, respectively. The symmetry of the annular gas jet in the absence and presence of spray is demonstrated here at different axial locations. Apart from the obvious decay and spread of the jet with increasing downstream distance, the significant spread of the swirling jet compared with its non-swirling counterpart is evident. In addition, the increase in the difference between the mean velocity of the gas jet in the absence and the presence of the spray can be noted as the gas jet evolves downstream. Modarress *et al.* (1984), Shuen *et al.* (1985) have previously attributed this to the presence of fully or partly responsive particles in a turbulent gas jet, whereby there is a mean slip of particles that leads to momentum transfer to the gas from the particle phase. Since $St_d > 1$ near the atomiser for many droplets, it is understood that the primary momentum transfer occurs here from the gas phase to the liquid phase, in addition to part of the gas kinetic energy being utilised by the spray formation mechanisms.

A summarised version of the profiles is illustrated through the jet centreline decay and spread. Figure 3(*b*) shows the inverse centreline axial velocity of the gas jet, $u_{x,0}(x) = u_x(x, r = 0)$ normalised with the exit gas velocity, U_g. In single-phase gas-jet measurements $u_{x,0} \propto (x - x_0^{u_x})^{-1}$ beyond the developing region ($x/d_g \geqslant 7$), where $x_0^{u_x}$ is the virtual origin based on the decay rate of the jet's centreline velocity. In order to quantify this evolution and also compare the changes in the presence of spray, we calculate the centreline profile as defined by Panchapakesan & Lumley (1993), Lau & Nathan (2014), Huck *et al.* (2022):

$$\frac{U_g}{u_{x,0}} = \frac{1}{B}\frac{x - x_0^{u_x}}{d_g}, \tag{4.1}$$

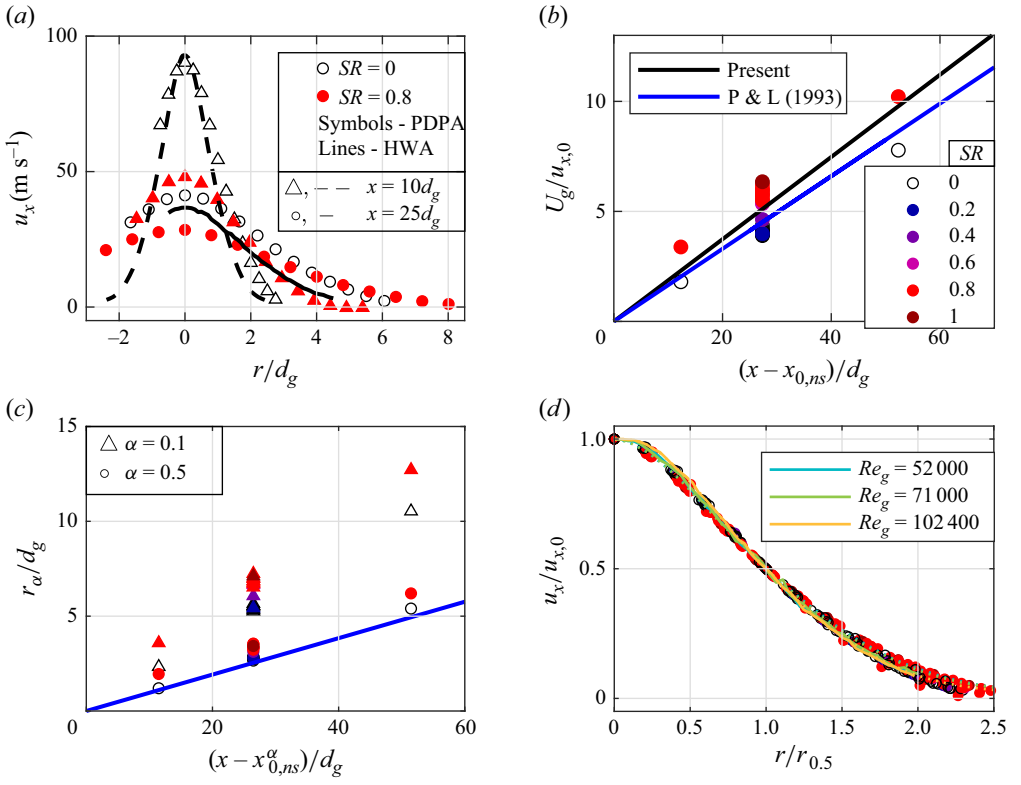

Figure 3. Gas-phase mean axial velocity (u_x) characterisation in spraying (PDPA) and non-spraying conditions (hotwire anemometry, HWA). Non-swirling flow conditions are indicated by open markers from PDPA measurements (conditioned on only droplets whose size is below 5 μm) and swirling conditions are shown in filled markers. (*a*) Comparison of the PDPA (symbols) and hotwire anemometer (lines) radial profiles of the mean axial velocity at $x/d_g = 10$ (△ and - -) and 25 (○ and –) for $Re_g = 102\,400$. For PDPA, red filled symbols indicate swirled sprays. (*b*) Longitudinal decay of the centreline mean axial velocity along the axial distance, identifying one virtual origin ($x_{0,ns} = -2.4d_g$) for $SR = 0$ and using the same for all other conditions ($SR > 0$). The gas flow statistics obtained from all Re_l and Re_g (listed in table 1) are added with different colours depending on their SR value. The same convention is used for the rest of the panels in this figure and figure 5. The blue line is from the round jet experiments of Panchapakesan & Lumley (1993). (*c*) Spreading of the annular gas jet displayed using the non-dimensional half-width (○) and the 10 % width (△). Here, $x^\alpha_{0,ns}$ represents the virtual origin corresponding to $\alpha = 0.5$ or 0.1 for $r_{0.5}$ and $r_{0.1}$. (*d*) Normalised mean axial velocity as a function of the non-dimensional radial coordinate $r/r_{0.5}$. The displayed conditions span all Re_g, Re_l and SR values from table 1, as well as all the explored longitudinal locations x. The dashed and solid underlying lines represent data obtained using hotwire anemometer at both $x/d_g = 10$ and 25.

where $1/B$ is the average decay rate and $x_0^{u_x}$ is the virtual origin associated with it. Different values of the gas jet's parameters from the literature are provided in table 2. We observe a small deviation of the single-phase gas jet (black line) from the data of Panchapakesan & Lumley (1993) (blue line). This difference may be due to the fact that while the present configuration is an annular gas jet, the experiments of Panchapakesan & Lumley (1993) consider a round jet. A higher decay rate of the annular gas jet agrees with the results of Kuhlman (1987) as shown in table 2. Moreover, measurements of gas flow from the spray droplets point to a decrease in its decay rate in the case of a non-swirling spray, indicating a modification of the carrier phase flow. The observations of Huck *et al.* (2022) regarding the decay of the gas jet, therefore, are closer to the observations of Panchapakesan & Lumley (1993); however, this is an outcome of a trail

Authors	B	$x_0^{u_x}$	$S_{0.5}$	$x_0^{0.5}$	$S_{0.1}$	$x_0^{0.1}$	$\theta_{0.5}^{u_x}$	$\theta_{0.1}^{u_x}$
—	—	(cm)	—	(cm)	—	(cm)	(deg)	(deg)
Panchapakesan & Lumley (1993)	6.1	0	0.096					
Huck *et al.* (2022)	6.7	−2.4	0.093	−3.8	0.182	−2.6	10.6	20.6
Kuhlman (1987) (Round jet)	6.9	−2.2						
Kuhlman (1987) (Annular jet)	4	−4						
Current (PDPA)	6.7	−2.3	0.104	−1.5	0.202	−1.6	11.8	22.8
Current (Hotwire)	5.4	0.4						

Table 2. Comparison of the jet decay and spread constants for a single-phase jet and in the presence of spray from (4.1)–(4.3). Note that here $d_g = 1$ cm.

of physical phenomena. Combining the information that an annular jet yields a bigger decay rate value than a round jet (Kuhlman 1987) and that, for particle-laden coaxial jets for similar mass loading, adding particles to a jet decreases its decay rate (Park & Chen 1989), our observations, with different decay rates in single- or two-phase conditions are in good agreement with the literature accounting all the physical traits.

For a swirling spray, there are significant deviations from the non-swirling case. The possible deviations are in virtual origin, decay rate and spreading rate. While the limitation of the data does not reveal the virtual origin ($x_{0,SW}$), it indeed points to an increase in the decay rate of velocity with an increase in SR. Such an increase is a consequence of the increased length scale associated with the swirling motion for a given axial transport of both the dispersed and continuous phases. More consequences of this behaviour will be elaborated in the sections ahead.

The conservation of momentum of a turbulent jet necessitates a linear increase in the jet width as it evolves downstream. To represent this spread, the half-width ($r_{0.5}$), which is the radial location where $u_x = 0.5u_{x,0}$, is identified. This radius is related to the axial distance through

$$r_{0.5} = S_{0.5}\left(x - x_0^{0.5}\right), \tag{4.2}$$

where $S_{0.5}$ is the spreading rate at the half-width and $x_0^{0.5}$ is the virtual origin corresponding to the jet half-width. In addition, with a similar definition, the ten-per-cent width ($r_{0.1}$) is also calculated. This radius is considered the jet edge on many occasions and is the location where entrainment plays a significant role. Figure 3(c) illustrates both radii. It is observed here that due to the increase in the decay rate with the increase of swirl in the gas jet, there is also an increase in its spreading rate. This is somewhat inferred from the $r_{0.5}$ plots and vividly from the $r_{0.1}$ plots. The jet angles, which are direct representatives of spread, are obtained from the evolution of r_α, with $\alpha = 0.5$ and 0.1, as

$$\theta = 2\tan^{-1}(S). \tag{4.3}$$

The different values obtained for the annular gas jet with spray are close to the reported constants of Huck *et al.* (2022). Therefore, the present results extend the investigation to swirling sprays. A quantitative assessment of this angle ($\theta_{0.1}^{u_x}$) for the swirling gas jet of $Re_g = 102\,400$ with $SR = 0.8$ indicates an approximate increase by 25 % from the corresponding non-swirling condition (from 11.59° to 14.55° half-cone angle). As there is very small difference in the spread of $SR = 0.8$ and 1, figure 3(c) confirms that the 25 % increase of θ is reached gradually along increments of SR values (except for $SR = 0.2$ which resembles a non-swirling spray, in agreement with previous work). A similar

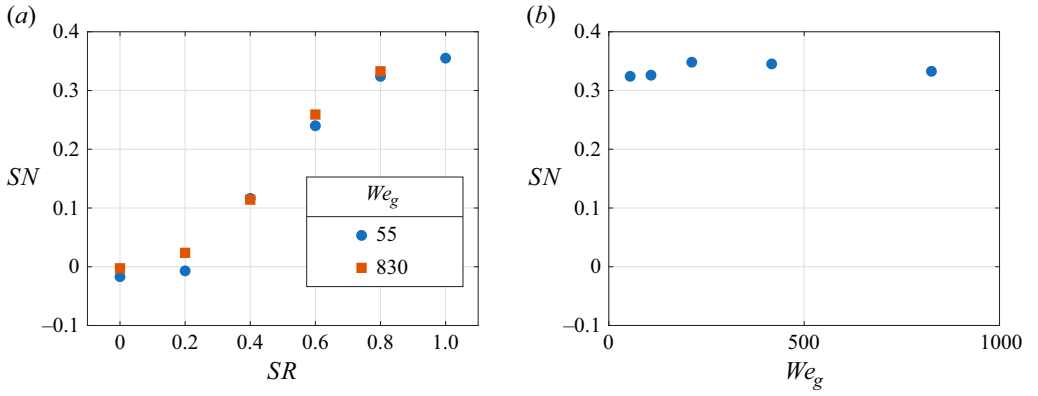

Figure 4. The swirl number SN calculated using (4.5) and plotted with the swirl ratio SR for two We_g values (a) and along We_g at $SR = 0.8$ (b).

behaviour is also observed for $\theta_{0.5}$, the jet angle based on 50% centerline velocity. While the spreading rate of swirled spray may slightly vary with the gas Reynolds number, it is first and foremost determined by the value of SR.

For a round gas jet, the radial and axial variation of u_x is well accommodated using a self-similarity curve often given by

$$\frac{u_x}{u_{x,0}} = \exp(-C\eta^2), \tag{4.4}$$

where $\eta = r/(x - x_0^{u_{x,0}})$. The self-similar variable η has a corresponding value in $r/r_{0.5}$ with a scale ($S_{0.5}$) to recover the same shape. In light of this understanding, a similar nature for different conditions with respect to the $r/r_{0.5}$ coordinate is illustrated in figure 3(d). It includes non-swirling as well as swirling conditions for different axial locations. There is an appreciable collapse across all the cases of table 1. This collapse is indicative of the axial momentum-conserving nature of the jet, even in the presence of a swirl. However, critical information for a swirling spray also underlies other velocity components of the carrier phase, pertinent to determining the drop size and liquid mass distributions in a particular spray plane.

4.2. *Mean radial (u_r) and tangential (u_θ) velocity of the jet*

It is important to discuss here that the swirl ratio SR is a proxy parameter for quantifying the swirl. As the values of u_θ and u_x are not a constant value over the annular gap of the nozzle, an integrated approach until the maximum measurement radius, r_{max} is used to better characterise the swirl intensity by calculating the swirl number (SN), given by

$$SN = \frac{\int_0^{r_{max}} 2\pi\rho_g u_x u_\theta r^2 \,\mathrm{d}r}{r_{max}\int_0^{r_{max}} 2\pi\rho_g u_x^2 r \,\mathrm{d}r}. \tag{4.5}$$

Here, SN represents the ratio of the axial flux of the angular momentum to the axial flux of the axial momentum. This definition follows that by Beér & Chigier (1972) and has been mentioned to be applicable for the characterisation of swirl generated through different mechanisms, such as vanes, helical structures, and also by inlet-based methods (like in the present studies). The appropriateness of this parameter can be clearly observed in figure 4, which plots SN at the nozzle exit with respect to SR. The measurements are conducted 1 mm away from the atomiser using PDPA with olive-oil-based smoke with sizes of the

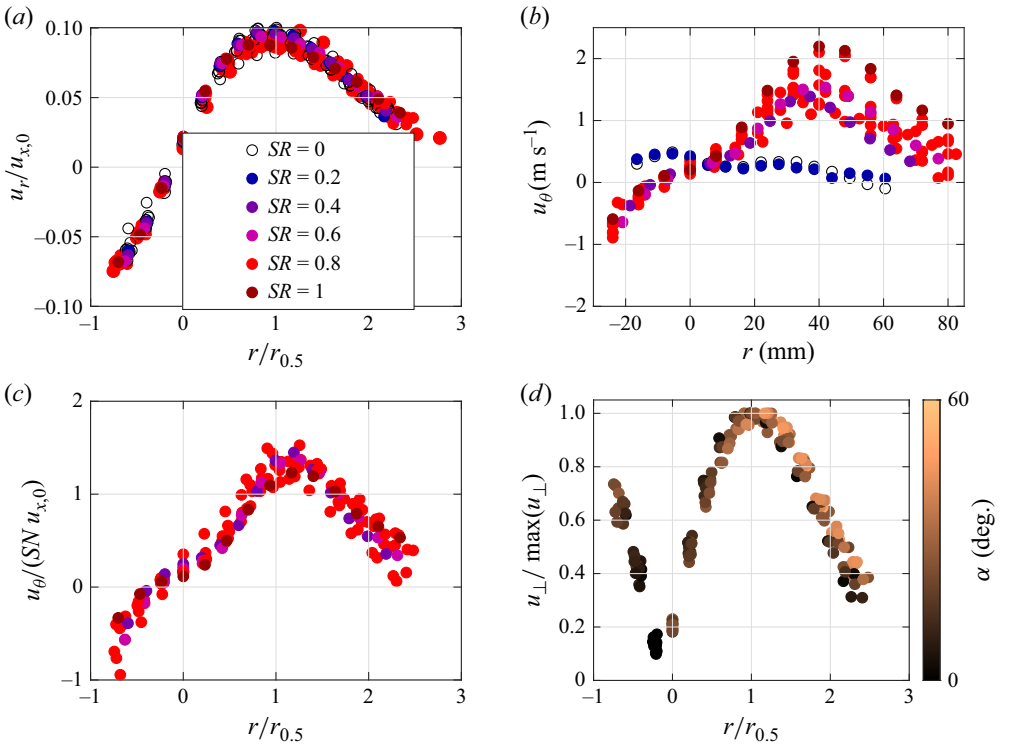

Figure 5. Gas-phase radial velocity (u_r) and tangential velocity (u_θ) characterisation. All the non-swirling conditions are shown with black open circles, and swirling conditions are shown with filled circles of different colours depending on *SR*. (*a*) Radial velocity profiles normalised with their centreline axial velocity shown as a function of the radial coordinate non-dimensionalised with their half-widths of the axial velocity profiles for all the conditions in table 1. (*b*) Radial profiles of the tangential velocity for all cases in table 1. (*c*) The tangential velocity normalised with centreline axial velocity and *SN* (from (4.5)) as a function of non-dimensional radial coordinate for $SR \geqslant 0.4$ at $x/d_g = 25$ for all Re_l and Re_g. (*d*) Non-dimensional radial profiles of the normalised velocity in the $r-\theta$ plane for $SR > 0$ in table 1 for all Re_l and Re_g at $x/d_g = [25, 50]$. The colour map indicates the angle subtended by the $u_\perp$ with the u_r.

order of 1 μm. Figure 4(*a*) showcases the fact that irrespective of gas Weber number, *SR* characterises the flow as well as *SN*, and therefore can be used interchangeably for parameterisation. The broad span of We_g values reported here encompasses the range of the spray operations of this article. Figure 4(*b*) shows the relation between *SN* and We_g for $SR = 0.8$. It further reinforces the independence of SN/SR with the change in We_g. In what follows, *SR* is used throughout, being the controlled parameter, as it conveys the same level of information about the swirl intensity as *SN*.

Figure 5 demonstrates the mean radial (u_r) and tangential (u_θ) velocity components of the gas jet in the presence of spray, which are roughly one order of magnitude less than u_x. The self-similar behaviour of the radial velocity profile and its radial increase followed by gradual decrease is given by Pope (2001), calculated from the data of Hussein *et al.* (1994) using the continuity equation. A similar profile is also observed here for the non-swirling gas jet (figure 5*a*), although with a difference in scale as the continuity equation used by Pope (2001) will not provide exact values due to entrainment effects. In addition, we also observe the same profile shape for the radial velocity, even in the presence of some tangential motion in the gas flow. The measurements were restricted to the radial locations where there were enough droplets available for statistical convergence

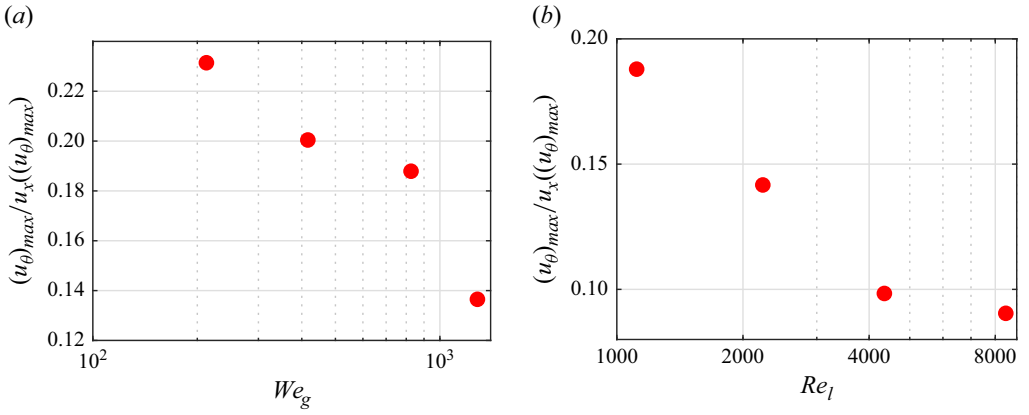

Figure 6. Swirl value of the gas phase calculated from the data for $SR = 0.8$ and $Re_g = 102\,400$ at $x/d_g = 25$.

(for acquisition times limited to 25 min). Nonetheless, the radial extrapolation of radial velocity profiles leads to a region of negative value, marking the entrainment region. This behaviour is observed not only for the non-swirling gas jet but also for the swirling jet.

In a swirling flow field, along with u_x and u_r, u_θ also contributes significantly to the droplet distribution due to its contribution towards the centrifugal force. Figure 5(*b*), therefore, demonstrates the radial behaviour of the tangential velocity, which establishes the fact that the spray encounters a meaningful tangential velocity only when $SR \geqslant 0.4$. Hence, the comparisons of the characteristics of the swirling spray with the non-swirling spray are conducted primarily with $SR = 0.8$. The mean tangential velocities for conditions with $SR \geqslant 0.4$ at a particular axial location can be non-dimensionalised with a product of the axial location's centreline velocity and swirl number (SN) given by (4.5). This non-dimensional tangential velocity is plotted along the radial distance normalised by $r_{0.5}$. Figure 5(*c*) presents this profile, which is self-similar across different SR and flow conditions but not across axial locations. The definition of SN establishes that the relative angular velocity of the gas jet at different radial locations concerning the centreline axial velocity is nearly a constant factor defined by the ratio of axial flux of angular momentum and axial flux of axial momentum.

Although most of the momentum is in the axial direction, with a minor contribution from u_r and u_θ, together they can affect migration of the droplets which may result in a change in the dispersion behaviour of the droplets. To cater the lateral flow field in a combined manner, the velocity values in the perpendicular plane of the spray axis, given by $u_\perp = \sqrt{u_r^2 + u_\theta^2}$, are normalised by their maximum value and plotted with the radius non-dimensionalised with $r_{0.5}$ in figure 5(*d*). The profile is similar to non-dimensional u_r and u_θ profiles. In addition, the angles subtended by $u_\perp$ with u_r are high only for $r > r_{0.5}$. However, the converse may not always be true, as observed from the plot. It is observed that r_{crit}, the radial location where $u_\perp$ is maximal, roughly coincides with $r_{0.5}$. The self-similarity of $u_\perp$ and u_x establishes a conserved nature of the spray, independent of swirling intensity, whereby appropriate identification of the similarity parameters can result in the unique description of the spray, irrespective of condition and location.

Until now, the mean velocity profiles have mostly been normalised with centreline axial velocity. However, a better essence of the swirling motion comes from its normalisation with the axial velocity for that location, which is shown in figure 6 along We_g and Re_l.

It indicates that, for a constant SR value, the swirling intensity of the gas decreases with increasing We_g as a higher swirling velocity at the exit of the nozzle is associated with high shear and a more considerable effective distance covered by the fluid particle, resulting in higher dissipation with respect to the axial motion. On the other hand, with an increase in Re_l, more kinetic energy is required for breakup and dispersion, which leads to a smaller contribution to the tangential velocity. It is important to note here that the mechanism of loss of the swirling motion with increasing We_g and Re_l are different. Consequently, the droplet dispersion at higher We_g and Re_l are affected differently, which will be elaborated in further sections.

4.3. *Droplet slip*

The gas phase on interaction with the droplets determines the latter's dispersion. A classical way of representation has been to investigate the slip of the big droplets in the surrounding gas phase. While particles with $St < 0.01$ are typically considered to behave as tracer particles (Balachandar & Eaton 2010), for a more optimistic determination of the gas phase, we consider $St < 0.002$ as a limit for identifying particles as tracers of the gas jet. On the other hand, the bigger particles with Stokes number, $St > 0.01$, are known to accumulate at regions of high strain rate (Eaton & Fessler 1994). As a result, particles in a high-speed jet exhibit some slip relative to the carrier flow. In a polydispersed spray, the size of droplets varies widely, resulting in $St_d \sim 10^{-4}$ at the nozzle exit for the present investigation, where the subscript d indicates droplet here. Considering that the droplets for which $St_d > 0.005$ are either partially responsive or non-responsive, we investigate the slip behaviour of these droplets in figure 7. To find this slip velocity (U_s), we first compute the size class of droplets that yields $St_r > 5 \times 10^{-3}$, defining a local Stokes number where the flow time scale is based on the radius of the location (r) as length scale divided by the mean local gas axial velocity. This formulation leads to a radial increase in the average drop size used in the definition as the location is farther from the jet centre which is shown in figure 7(*a*,*b*). Therefore, U_s is limited to the radial location for which $d_{|St_r>0.005} < 100$ μm, since this corresponds to the biggest drop measured. Then, we find the average axial velocity of these droplets for which $d_{|St_r>0.005} < d < 100$ μm and calculate the difference from the gas mean axial velocity $U_s(r) = \langle v_{x|St_r>0.005}\rangle(r) - u_x(r)$. Note that from here, plots with open and filled markers will represent $SR = 0$ and $SR > 0$, respectively.

Compared with the gas flow, the big droplets in a non-swirling spray accelerate, overshoot the gas flow, and then decelerate as they transport downstream (Lasheras & Hopfinger 1998; Wu *et al.* 2022; Zhou *et al.* 2022). At $x/d_g = 25$, $U_s > 0$ at the centreline, as noticed in figure 7(*c*,*d*), which is either in the overshoot or deceleration region. This is in confirmation of the results on PLJs (Hardalupas, Taylor & Whitelaw 1992) and sprays (Lasheras *et al.* 1998). The slip velocity, U_s, increases with radius from the centreline and decreases after reaching a maxima. The radial profiles observed here are similar to the trends observed by Wu *et al.* (2022) in sprays and can be interpreted from the results of Zhou *et al.* (2022) on PLJs. The reason for an off-centre maximum is the higher particle inertia of the large droplets, which leads to high velocity far downstream while the gas jet spreads more rapidly, thereby decaying faster (Gounder *et al.* 2012). Eventually, when $r/r_{0.5} > 1$, the Stokes number experienced by the big droplets becomes small enough to attain a velocity value close to that of the gas phase. These results are also complemented by the fact that U_s decreases with higher Re_l closer to the centreline (figure 7*c*) and is indicative of the late response of the big droplets, which occurs at farther downstream distance from the exit of the atomiser. Therefore, the inertia attained is also low.

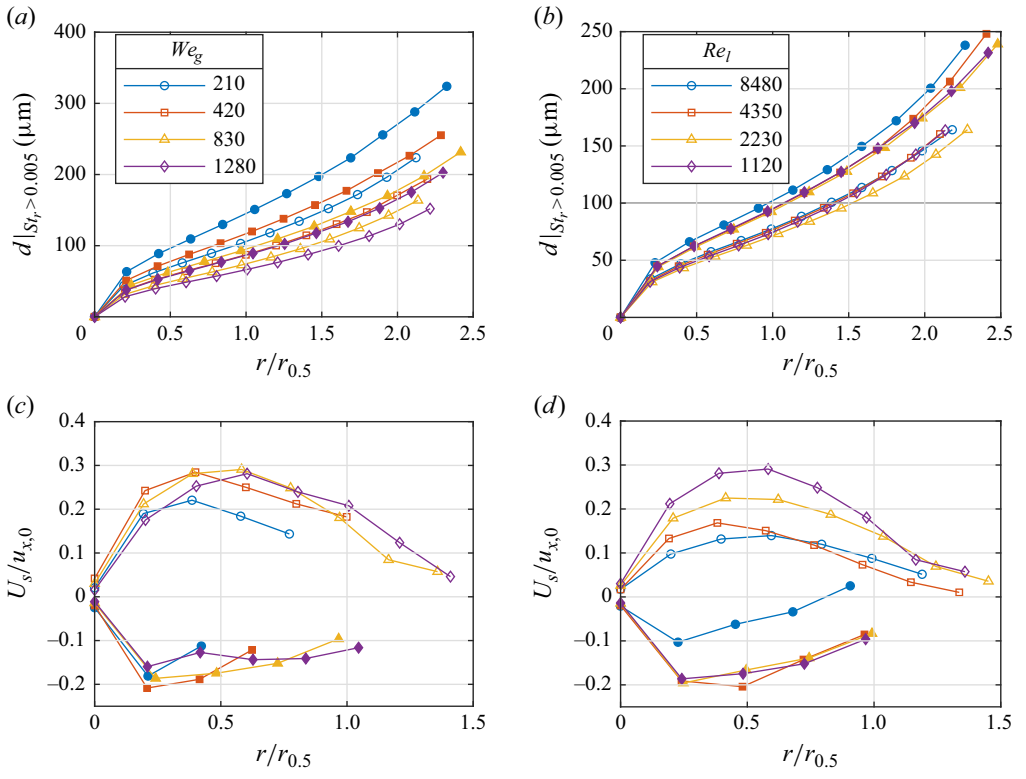

Figure 7. Radial profiles for the computed average size of drops whose local Stokes number respects $St_r > 0.005$ with varying (*a*) We_g and (*b*) Re_l for swirling (open markers) and non-swirling (filled markers) conditions. The horizontal 100 μm line indicates the limit of droplet size measurement in this study. Radial profiles of slip velocity defined by the velocity difference of droplets with $St_r > 0.005$ and $u_{g,x}(r)$ for different (*c*) We_g and (*d*) Re_l.

With swirl added to the gas jet, the increase in spreading leads to a reduced mean axial velocity of the carrier flow, however, much smaller than that found for the droplet velocities. As a result, figure 7(*c*,*d*) demonstrates that $U_s < 0$ for most radial locations accessible here, reaching a minimum before increasing again with the radius. In addition, no specific correlation was observed with We_g or Re_l. Considering droplets that are centrifuged away from the jet's centreline, carrying high axial momentum accumulated there and carried over to regions of $r > 0$, one may expect droplet velocities larger than that of the carrier flow. On the contrary, droplets that are formed by high-amplitude flapping events, commonly found in swirled sprays, are ejected directly outside of the gas jet and may find their way back to the jet only due to entrainment, explaining their low axial velocities. Combining these statements, the averaged droplet velocity is found largely to be smaller than in non-swirling conditions, indicating that there may be a larger proportion of initially detrained droplets that are then entrained back into the jet than droplets centrifuged from the jet's axis. An exception is the $Re_l = 8480$ condition displaying a lower negative amplitude of U_s. In comparison with the other conditions, the high-momentum liquid jet may in that case produce more large droplets in the vicinity of the centreline whose high inertia better preserves their axial momentum as they get centrifuged radially, leading to positive slip velocity close to $r = r_{0.5}$.

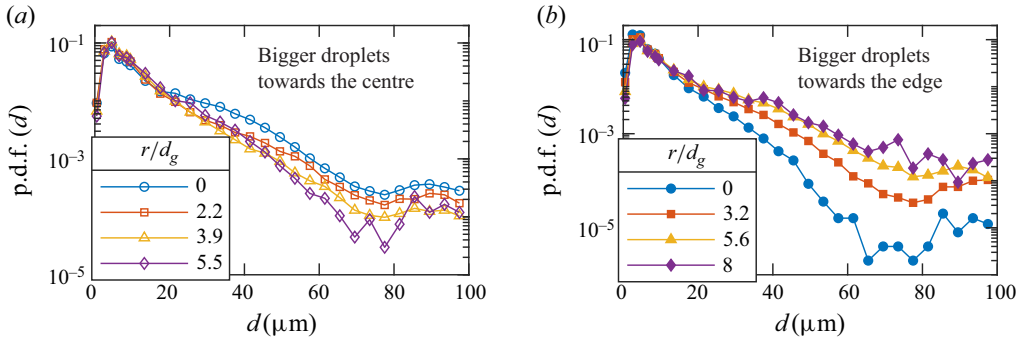

Figure 8. The p.d.f. at several radial locations for a given longitudinal distance $x/d_g = 25$, for $Re_l = 1120$ and $We_g = 830$ at (*a*) $SR = 0$ and (*b*) $SR = 0.8$.

5. Droplet size distribution

An essential component of characterising any spray is deciphering the drop size variation with different governing parameters. To address this, we focus on a point-wise and a global statistical description of the spray. These assessments will help to take a step towards characterising the spatial description of the liquid mass distribution. We want to point out that the present measurements are restricted to a drop size up to 100 μm.

5.1. *Local drop size characteristics*

A noteworthy feature of coaxial sprays is the production of drops with a wide range of sizes, which one can assess from the droplet distribution plots shown in figure 8. While the peaks of the distributions are found below 10 μm, the mean droplet size can vary with radial location by typically tens of μm, depending on the condition (not shown here). The 70–100 μm range is found to approximately plateau for most conditions and locations as shown in figure 8.

The spray formation mechanism explained for high We_g (Marmottant & Villermaux 2004; Huck *et al.* 2022) leads to larger mean droplet size in the centre of the spray than at the edge in the absence of swirl. We show the probability distribution functions (p.d.f.s) of drop sizes for such a condition for a fibre-type atomisation regime at different radial locations for a non-swirling spray in figure 8(*a*), which confirms the established understanding. An addition of swirl (shown in figure 8*b*) can be observed to reverse the spatial sampling of droplets in the spray, with smaller droplets found at the centre. This change indicates the manipulative influence of the centrifugal force in rearranging droplets in a spray plane, based on their mass ($F_c = m_d\omega^2 r$, where m_d is the mass of droplets and $\omega = u_\theta/r$), and hence size. Such behaviour contributes to an increase in the spray angle beyond the gas jet angle for a swirling spray as the large droplets are flung far due to F_c (Préaux *et al.* 1998). This explanation is complemented by the smaller eddy turnover time near the toroidal region close to the atomiser for high swirling flows, due to which only the small droplets that have a small response time are entrained. This argument also holds good for conditions with low We_g. However, as the mechanism of droplet breakup and entrainment in low-We_g conditions favour the same organisation of droplets with and without swirl, no change is noticeable with such a representation and will require a different description, which we provide later in the following subsection.

On the other hand, for low-We_g conditions, the origin of droplets of different size ranges varies, and hence their dynamics differs in the carrier phase. Chigier & Farago (1992)

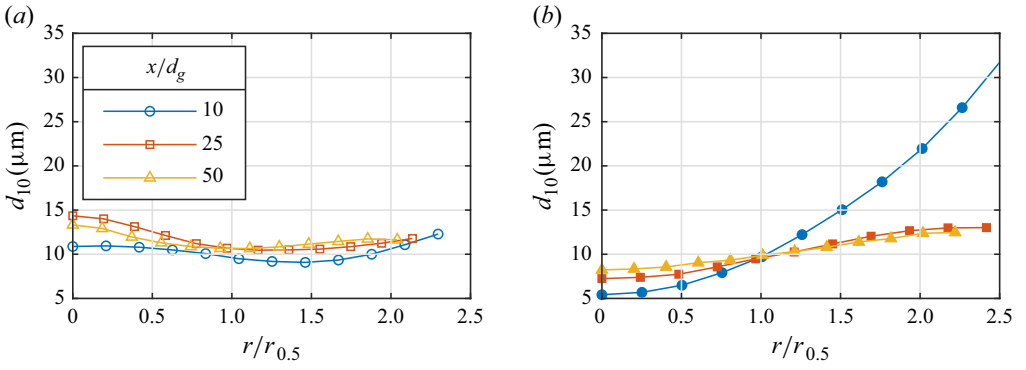

Figure 9. The mean droplet size (d_{10}) plotted with radius non-dimensionalised with $r_{0.5}$ for $Re_l = 1120$ and $We_g = 830$ at various axial distances x/d_g. (*a*) $SR = 0$ and (*b*) $SR = 0.8$.

have reported that liquid jet breakup with low We_g, and hence low Re_g, is a regime where atomisation predominantly occurs through the formation and bursting of bags, contributing to forming much finer droplets than expected at these We_g values (if bags were absent). Its rims and ligaments form large droplets, following similar processes as for the breakup of a single droplet subjected to a gas flow. In addition, due to the flapping behaviour of the liquid jet at these low We_g, the outward ejections of large droplets result in a droplet distribution peak $\sim$100 µm at the spray edge. Calculating the Weber number of these big droplets based on slip velocity, the value obtained is less than 1, indicating no further breakup of these drops is possible. It is well known that the spread of a gas jet results in mass entrainment. While droplets with $St < 0.01$ can certainly respond to entrainment and attain an inward radial velocity, the droplets with $St > 10$ have a ballistic motion. This behaviour is distinguishable primarily near the atomiser, where the breakup occurs. Combining these understandings points to the fact that only finer droplets can get influenced by entrainment ($\propto u_x$) and have a higher probability of accumulating near the centre of the spray. Therefore, the droplet distribution favours small droplets at the centre and large ones at the edge (not shown) for low We_g. This understanding confirms the results obtained by Huck *et al.* (2022).

Figures 9(*a*) and 9(*b*) shows the radial profiles of the mean drop size at different axial locations for high-We_g non-swirling and swirling conditions, respectively. These measurements reveal two aspects of spray development as droplets travel downstream in a turbulent environment. In the case of non-swirling and swirling sprays, we observe that at high We_g for $x/d_g = 25$ and 50, the drop size profiles are almost identical, indicating the fully developed nature of the spray. Comparing these profiles with the profiles at $x/d_g = 10$, two completely different behaviours can be observed for non-swirling and swirling conditions. For the non-swirling condition, one can observe a slight increase in the drop size throughout the spray with almost the same shape as observed at $x/d_g = 25$ and 50. This indicates a very minor rearrangement due to entrainment, but mostly coalescence of the droplets throughout the spray. On the other hand, for a swirling spray, the profile changes drastically, crossing the other two profiles at $r = r_{0.5}$, with drop size at the spray's edges more than double the values found farther downstream. The profiles change from the centrifugal sorting near the atomiser to homogenisation due to turbulence far from the nozzle. Therefore, we conduct further investigations on the radial profiles of the drop size at $x/d_g = 25$, by which time the radial profiles have evolved to a fully developed profile for all conditions.

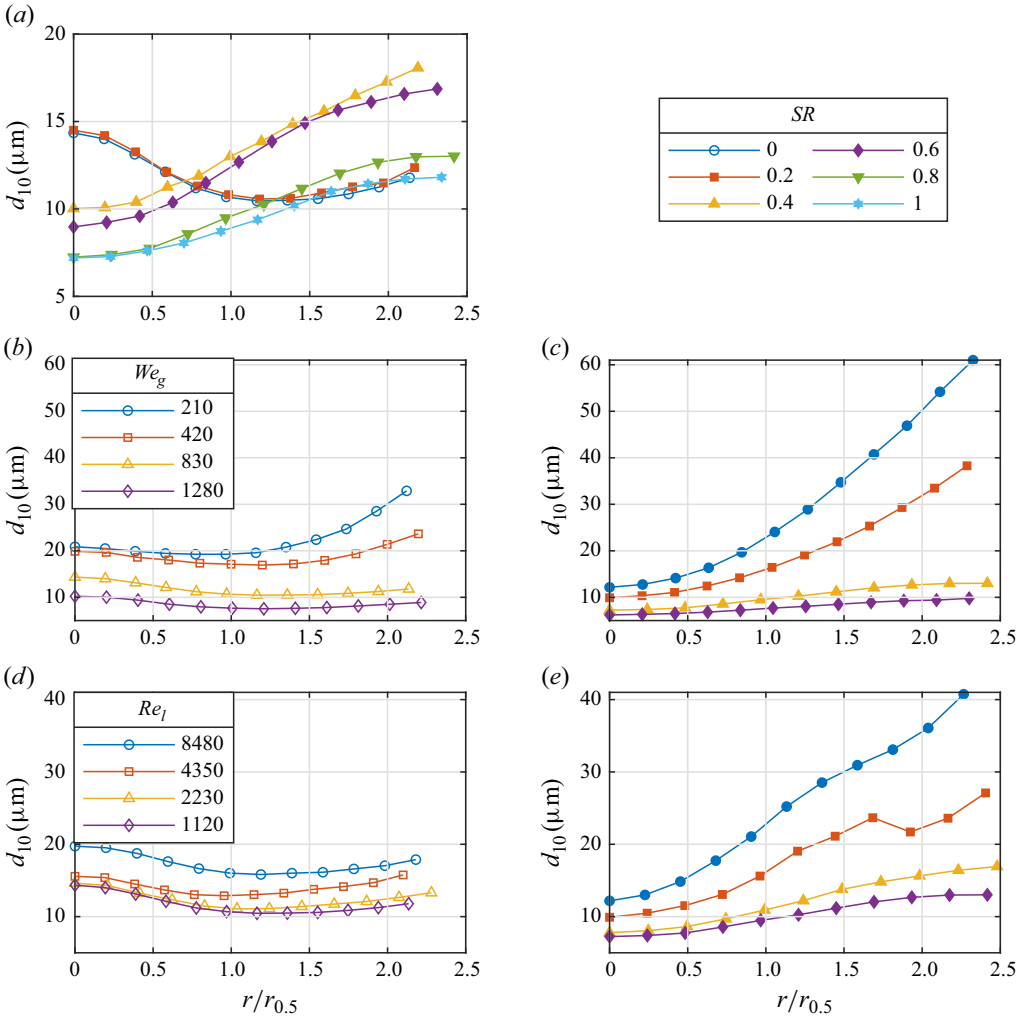

Figure 10. The mean droplet size (d_{10}) plotted with radius non-dimensionalised with $r_{0.5}$ for different flow conditions at $x/d_g = 25$. (*a*) $We_g = 830$, $Re_l = 1120$ for different SR values. (*b*,*c*) Fixed $Re_l = 1120$ at different We_g values. (*d*,*e*) Fixed $We_g = 830$ at different Re_l values. (*b*,*d*) $SR = 0$. (*c*,*e*) $SR = 0.8$.

Figure 10 demonstrates the influence of different parameters on the radial variation of the mean drop size for a non-swirling and a swirling spray. A logical way forward is first to understand the influence of various swirl intensities and then downsize the investigation to a few conditions. Therefore, figure 10(*a*) highlights the changing nature of the mean droplet size radial profiles with increased swirl intensity. Such a radial variation of the drop size (albeit for the Sauter mean diameter d_{32}) is also observed by Préaux *et al.* (1998) and (for d_{10}) by Fong *et al.* (2024). The invariance of the profile for $SR < 0.4$ is in confirmation to the inference obtained from figure 5(*c*) that there is a limited effect of swirl in such cases. The radial d_{10} profile changes from a '$\sim$' shape at negligible swirl values to a '$\cup$' shape when the swirl effects exist. To quantify this change we describe a two-location identifier of the shape d_{10} at $r/r_{0.5} = 1:2$ (normalised by the value at $r = 0$) given by [a b]. Measuring the shape identifier for the conditions in figure 10(*a*), we find that this value changes from [0.74 0.8] for $SR = 0$ to [1.24 1.61] for $SR = 1$. When the

radial profile shape is '∼', as in the former condition, the shape identifier value decreases slightly (from 1 to 0.74 here) and then increases (from 0.74 to 8 here). For a '∪' profile, as in the later condition, the value increases monotonously with larger relative amplitudes (1, 1.24 and 1.61 here). For $SR \geqslant 0.4$, one can observe in addition a decrease in the drop size with increasing swirl throughout the radial extent of measurements. This behaviour can be attributed to the increased probability of the small droplets closer to the centre and an indication of a decrease in the overall size of the droplets with increasing swirl for high We_g. These results are in agreement of the findings of Fong *et al.* (2024).

Figures 10(*b*) and 10(*c*) compare the effect of swirl on drop size for different We_g without and with swirl. The drop size decreases throughout a particular spray plane with an increase in We_g, irrespective of the swirl. However, a closer look at the radial drop size profiles for non-swirling sprays (figure 10*b*) suggests that the shape identifier value changes from [0.92 1.4] for $We_g = 210$, indicating almost a '∪' shape with very high values at the edge, to [0.75 0.83] for $We_g = 1280$, indicating a '∼' shape. For swirling conditions (figure 10*c*), this profile retains the '∪' shape for all We_g due to the explanation given earlier. Nonetheless, the curvature of the profile, i.e. the steepness of the radial increase in mean droplet size, can be observed to decrease with the increase in We_g for the later conditions. The change is especially striking for the two higher-We_g values, such that the drop sizes do not deviate significantly in all the spatial domains and are in the closer range found for non-swirling sprays. The shape identifier value varies from [1.88 4.14] for $We_g = 210$ to [1.22 1.51] for $We_g = 1280$, indicating the drastic change in the magnitudes of the radial variations making the spray much more homogeneous in terms of droplet size (going from a fourfold to a 50 % increase only). These results lead to the inference that three factors contribute to defining the shape of the droplet size radial profiles: (i) the higher gas kinetic energy with increasing We_g leading to the formation of smaller droplets, which are influenced by entrainment, (ii) the increase in the unfavourable pressure gradient with increase in u_θ and (iii) the independence of critical swirl number, S_c from M at high M (Hopfinger & Lasheras 1996). Altogether, these factors reduce the preferential segregation of droplets for higher We_g. Nevertheless, a subtle difference in the radial profile from the '∪' shape is the change from a monotonic increase without noticeable inflection point ($(\mathrm{d}^2d/\mathrm{d}r^2) \geqslant 0$) at low We_g to the presence of profiles with inflection point ($(\mathrm{d}^2d/\mathrm{d}r^2) = 0$) at higher We_g, either side of which the curvature changes sign.

While a similar investigation for two values of We_g on radial drop size profiles has been demonstrated recently by Fong *et al.* (2024), an investigation into the effect of Re_l on a non-swirling spray is elaborated here. Figure 10(*d*) shows that although there is a change in the magnitude of radial drop size profiles with increase in Re_l, there is barely any change in its shape, contrary to the effect of We_g. For the non-swirling spray, the '∼' radial drop size profile varies from the shape identifier value of [0.81 0.87] at $Re_l = 8480$ to [0.74 1.1] at $Re_l = 1120$. This examination substantiates the significant role that We_g plays in the initial liquid jet breakup mechanisms over Re_l (Lasheras & Hopfinger 2000; Tolfts, Deplus & Machicoane 2023), leading to the drop size profiles. On swirl addition to the gas flow (figure 10*e*), the radial profiles are '∪' shaped. Specifically, this shape has a similar inflection for conditions with small-Re_l and large-We_g values. The associated shape factors are [1.87 2.92] for $Re_l = 8480$ and [1.32 1.76] for $Re_l = 1120$, indicating a significant change in the size between the edge and the centre. Focusing on both parameters indicates that the gas-to-liquid dynamic pressure ratio M may have a role in determining the drop size profiles for swirling sprays. However, our efforts in combining the effect of Re_l and We_g through M does not provide any direct correlation. This behaviour confirms that the relationship between drop size and the flow parameters is non-trivial. With more results, this aspect is elucidated further in § 7.

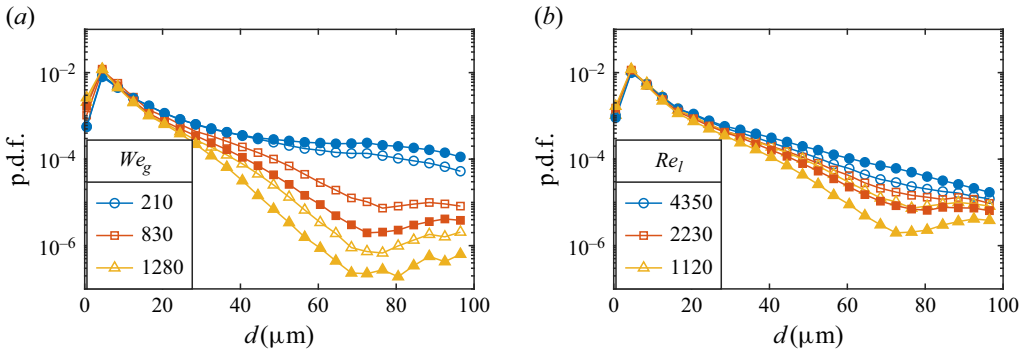

Figure 11. Global drop size distributions for different We_g for $Re_l = 1120$ (a) and Re_l for $We_g = 830$ (b), at $x = 25d_g$. Empty symbols correspond to non-swirling conditions while filled ones are for $SR = 0.8$.

5.2. *Global drop size characteristics*

Most of the literature has focused on a radial change of drop size, which is a point-wise measurement with a variable contribution to the global spray based on the radial location. Elaboration of this representation is shown through figure 1(d), where each cross represents the radial location and the annular space represents the area that each of these locations (blue annulus for one of the locations is highlighted as an example) is assigned to. Therefore, in order to make the contributions of each radial location a justifiable proportion of the global spray, we define a p.d.f. as follows (Tratnig & Brenn 2010; Dhivyaraja *et al.* 2019; Osuna Orozco 2021; Fong *et al.* 2024):

$$p_i = \frac{\sum_j N_{ij} S_j / w_i T_j}{\sum_i \sum_j N_{ij} S_j / w_i T_j}, \tag{5.1}$$

where N_{ij} is the number of particles in droplet size class i at location j, S_j is the area which the location j represents (figure 1d), w_i is the weight of the droplet size class i depending on the diameter of the probe volume, which is required for rectifying the bias due to the Gaussian nature of the laser beam and T_j is the time of collection of data at location j. The weighting function w_i is determined by fitting a logarithmic curve fitting between the drop size and the path length of the droplets in the probe volume. The cumulative p.d.f. is plotted for different We_g and Re_l in figures 11(a) and 11(b), respectively, for non-swirling and swirling sprays. One can notice that at low We_g and high Re_l, there is a higher probability of bigger droplets for the swirling spray compared with the non-swirling one, and the converse is true for high We_g and low Re_l. However, when swirl assists the spray (e.g. at high We_g and low Re_l) the reduction in the probability of large droplets is massive, with for instance a probability decrease of a factor of roughly 3–5 in the 50–80 µm range. The resulting drop size (d_{10}) from (5.1) is shown in figure 12. One can observe a decrease of drop size with the increase in We_g and the converse with increasing Re_l due to the increased inertia compared with the surface tension forces with increasing M. While the spread of the spray due to swirl is well known, this analysis gives a global assessment of the drop size. We conclude that swirl reduces the drop size for high M. However, it may have a detrimental effect in terms of drop size at lower M. The recently presented results on the mean drop size by Fong *et al.* (2024) claims that there is a monotonous decrease in the size for the whole spray droplet size with the introduction of swirl for $M = 25$ and 56, and hence for all regimes of spray. However, the present exploration to further lower M and also different Re_l values indicates a complicated relation between the global drop size

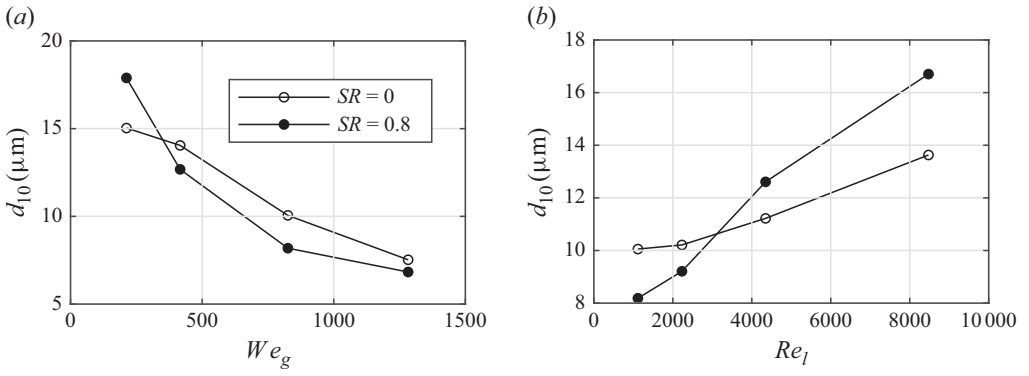

Figure 12. Variation of the global mean drop size d_{10} with We_g for $Re_l = 1120$ (a) and Re_l for $We_g = 830$ (b), at $x = 25d_g$. Empty symbols correspond to non-swirling conditions while filled ones are for $SR = 0.8$.

depending on Re_l, We_g and SR. In this way, the present result extends the existent findings on findings of Fong *et al.* (2024) on the effects of gas swirl on drop size.

6. Dispersion

Although the carrier phase and the drop size descriptions provide a significant understanding of the spray, these assessments are incomplete without realising how the liquid mass flow rate gets distributed in a spray plane. Therefore, in this section, we comprehensively assess the influence of the characterised carrier phase and deciphered drop size variations on the spatial liquid volume distribution. This quantity is best explained through dispersion, which includes characterising the fluxes, and its relative response in the carrier phase gas flow. This section will help us relate different observations of the swirling spray to the existing understanding of non-swirling sprays.

6.1. *Axial flux*

The preceding discussion on gas-phase velocity and drop size have elucidated two important features of the swirling spray: (i) high axial gas velocity at the centre of the spray (figure 3) and (ii) large droplets at the edge of the spray (figure 10). Individually, they do not inform whether the mass flux will be high at the centre due to high velocity or at the edge due to the large droplet size, which is essential to assess liquid mass distributions. Therefore, we calculate the volume flux of the liquid at a particular location by

$$\dot{g_x} = \frac{\pi}{6T} \sum_{i=1}^{D} \sum_{j=1}^{N_i} \frac{d_{j,i}^3 \cos(\theta_j)}{\mathcal{A}_i}, \tag{6.1}$$

where T is the collection time (at the measurement location), $d_{j,i}$ is the size of the jth drop in the ith bin and $\theta_j = \tan^{-1}(u_r/u_x)$. Here, $\mathcal{A}_i$ is the size-dependent probe area given in (2.1). Figure 13 illustrates the influence of different flow parameters on the radial profiles of axial volume fluxes ($\dot{g}_x$), non-dimensionalised by their centreline values. For a non-swirling flow, the narrowing of the volume flux profiles with increasing We_g has been reported earlier by Hardalupas & Whitelaw (1994), Huck *et al.* (2022), which is also observed here. In addition, we observe opposite trends with an increase in Re_l, confirming the role of M in determining the axial flux profiles.

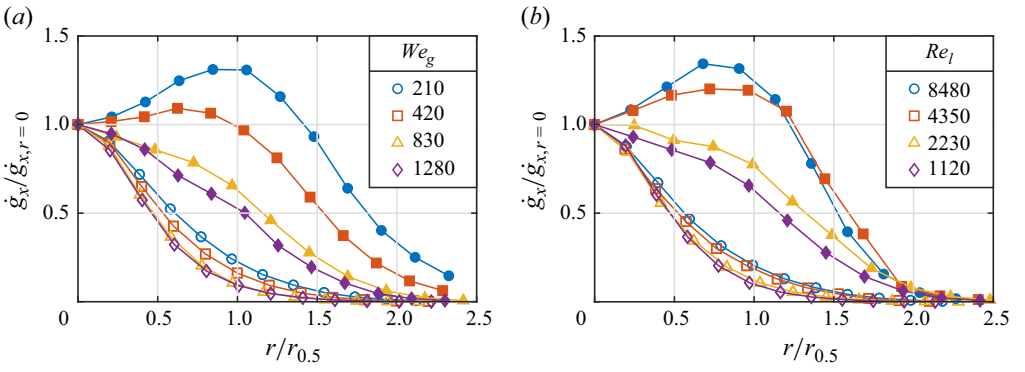

Figure 13. Radial profiles of axial flux with (*a*) $Re_l = 1120$, (*b*) $We_g = 830$ measured at $x = 25d_g$. Open and filled symbols represent the non-swirling and $SR = 0.8$ conditions, respectively.

On the other hand, although the volume flux profiles for the swirling flows follow a similar relationship with We_g and Re_l, they deviate from the bell-shaped radial profile. Especially for low-M values, the radial decrease is non-monotonic, and the maxima shifts away from the centreline, which is similar to the observations made by Fong *et al.* (2024) for the swirling conditions they investigated. In addition to these observations, the present investigation also highlights that depending on the liquid Reynolds number, in corresponding high-We_g conditions, the centreline can also have the maximum flux at a radial distance away from the spray axis. Note that our assessment does not associate a definitive M for this transition across varying Re_l, leading to a non-trivial relation of the change of shape of the radial flux profiles with M for swirling sprays.

The liquid jet breakup near the atomiser involves its orbiting about the axis of the atomiser when swirl is introduced (Machicoane *et al.* 2020; Kaczmarek *et al.* 2022). In the presence of this swirling gas, a large portion of the big droplets, and hence mass, are expected to centrifuge outside. However, the influence is predominant when the initial droplet formation happens sufficiently away from the axis, so adequate angular momentum is available. At low-M conditions, the orbiting liquid jet has a long length and will have a substantial propensity to break farther away from the axis and attain higher angular momentum, thereby shifting the maximum flux away from the centreline (found in the vicinity of $0.5 < r/r_{0.5} < 1$). Extrapolating this understanding to high-M conditions, due to very short breakup length in the case of high-M conditions, such a possibility is difficult due to the pre-existing high confinement effects close to the atomiser ($\propto U_g$). Nevertheless, the spread of the gas jet farther downstream and the corresponding transport of droplets facilitate the liquid mass to deviate away from the centreline due to the swirling motion of the gas, resulting in a broader bell curve, whose maximum is still located at $r = 0$. Whether swirled high-M conditions bear axial flux whose radial profiles can retain the shape of their non-swirling counterpart is unclear and would require more data, but the radial spread increases when swirl is impeded to the gas jet. This explanation can be complemented with the observations of Fong *et al.* (2024). Their results indicate that at a given gas-to-liquid momentum ratio M (with 25 and 56 sampled in their study), roughly similar shapes of radial volume flux profiles are observed through the gradual increase of swirl when its effect is noteworthy, with a clear broadening of the profiles. On closer inspection, high-swirl conditions present profiles that remain constant over a small subset of radial values (up to $2d_g$), before they decrease. We also observe similar results for low M in the same range of the parametric values as they examined. For higher-M conditions, adding swirl

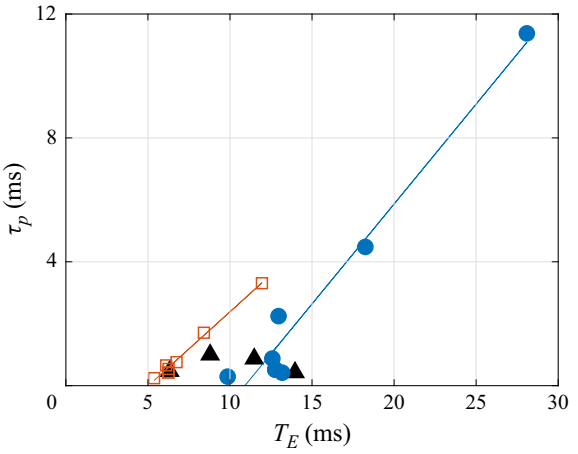

Figure 14. Droplet time scale based on mean size compared with the Eulerian time scale at the spray edge. The symbols □, △ and ∘ represent $SR = 0$, >0 and $=0.8$ conditions, respectively.

to the gas jet makes the profile wider but approximately retains the non-swirl shape across different $SR > 0.2$ values explored here. The combined understanding, therefore, is that the shape of the radial profile of axial fluxes are determined by the value of M even in the presence of swirl. Depending on the value of M, swirl may then change the shape of the profiles.

6.2. *Droplet response at the edge*

The spray edge is often considered an identifier of the spray formation method (Acharya *et al.* 2021; Huck *et al.* 2022). In addition, the response of specific-sized particles to particular eddies has been demonstrated, e.g. for shear layer by Lazaro & Lasheras (1992) and for gas jet by Chung & Troutt (1988), Longmire & Eaton (1992), Sbrizzai *et al.* (2004). The Eulerian time scale for these eddies is based on the large-scale helical structures existing in a gas jet and given by

$$T_E = 2r_{0.1}/u', \tag{6.2}$$

where u' is the centreline turbulent axial velocity fluctuation. The length scale $2r_{0.1}$ associated with this time scale for the jet is due to the correlation of the eddies with its width (Tso & Hussain 1989; Yoda, Hesselink & Mungal 1992), which we analyse at $r_{0.1} < r < r_{0.05}$ as its validity has been demonstrated throughout the jet cross-section by Prevost *et al.* (1996). The mean droplet diameter $\langle d_p \rangle$ at this radial location is used to calculate the time scale by

$$\tau_p = \rho_l \langle d_p \rangle^2 / (18 \nu_g \rho_g). \tag{6.3}$$

This relation is plotted in figure 14. The corresponding Stokes number is given by

$$St = \tau_p / T_E, \tag{6.4}$$

which is ∼0.1 or greater for all cases. These values indicate that the large eddies at the edge of the spray, which are evidenced both in non-swirling and swirling gas jets, will affect at least partially the droplets' trajectories, e.g. with the occurrence of radial ejections of the inertial droplets and loitering. In swirling conditions, these eddies are accompanied by helical structures that may play an additional role in spray dispersion. For non-swirling

sprays (red squares), the relation between large eddy time scale and mean droplet time scale is linear with varying conditions. This observation indicates that as the mean droplet time scale increases due to an increase in its size, so does the eddy size to which such drops can respond. The analysis of Huck *et al.* (2022) considers the peak droplet size in the distribution at the edge for varying axial locations for a single condition in a spray and the resulting Stokes number ~ 1 to claim the role of the helical eddies in transporting the big droplets by ejection. Their analysis was restricted for $M \lesssim 50$ when the ejections occurred. In contrast, the present analysis spans all We_g and Re_l values given in table 1. The present result underlines a universality of the droplet behaviour at the edge, irrespective of the regime.

Extending such an analysis to swirling sprays, we observe that with a gradual increase in SR, the large droplets at the edge respond to eddies of increasing time scales (as observed in figure 10) as traced from figure 14: the red squares representing $SR = 0$ are followed by black triangles going from left to the right of the plot representing $SR = 0.2$ to 0.6 until the blue circles. Subsequently, the circles are indicative of $SR = 0.8$, and, again, a triangle to its right is for $SR = 1$. The droplet versus the eddy time scale plot for $SR = 0.8$ (blue circles) is also observed to be almost linear like their non-swirling counterpart, although with a higher dispersion. Note that the helical structures in the case of swirling spray also have a contribution from the tangential component of velocity. The consequence is an increase in the time scale of axial fluctuations due to the eddies at the edge, which is larger than the droplet response time scale due to bigger drops.

7. Discussion and conclusion

After its role in the initial breakup of the liquid jet, the gas jet also bears significance in the droplet redistribution. At gas Weber numbers of 210 and 420, for the swirling conditions, the far-field swirl number value shown in figure 6 is greater than 0.2, indicating high swirling intensity at $r \approx r_{0.5}$. On the other hand, the drop size profile shown in figure 10(*b*) for the non-swirling condition has a '$\cup$'-shaped profile. Combining together these two observations, swirl addition in the gas jet leads to high intensity azimuthal velocities that make the radial drop size profile '$\cup$'-shaped without any inflection point. For all other conditions in figure 6(*a*,*b*), the far-field swirl value is less than 0.2, and as mentioned earlier, we observe that the shape of the radial profile of d_{10} remains driven solely by We_g, as the gas jet longitudinal momentum and its associated entrainment are the determining factors for such cases.

In addition to drop size radial profiles, the moments of the drop size for the whole spray can be assessed, yielding different characteristic diameters to quantify the influence of swirl (table 3). Considering the range of diameter that can be measured in the present configuration, this is limited to $We_g \geqslant 830$ to ensure that the entirety of the droplet size distributions are captured to prevent biases in estimating higher-order moments. Assessing the role of We_g from the first and third rows, we infer that not only d_{10} but also d_{32} and d_{43} decrease by roughly 25 % when the gas Weber number increases by 55 %. Such a synchronous change across different characteristic diameters indicates that the p.d.f. is roughly shifted as a whole towards smaller sizes. On the other hand, comparing rows 3 and 4, on gas swirl addition, while d_{10} decreases by roughly 10 %, d_{32} and d_{43} decreases by approximately 25 %, indicating that in addition to an overall droplet size reduction, the big drops are particularly affected by swirl and broken into smaller ones for this high-Weber condition. At a slightly smaller gas Weber number (rows 1–2), swirl addition more or less shifts the droplet size distribution to smaller sizes, with a reduction of the drop size moments of roughly 20 %.

Re_g	We_g	M	SR	d_{10}	d_{20}	d_{32}	d_{43}
102 400	830	90	0	10.06	14.33	35.11	49.81
102 400	830	90	0.8	8.18	11.59	28.46	42.1
127 700	1280	140	0	7.53	10.47	24.8	36.92
127 700	1280	140	0.8	6.83	9.26	20	28.49

Table 3. Different characteristic diameters $d_{nm} = [\Sigma p_i d_i^n / (\Sigma p_i d_i^m)]^{1/n-m}$ (in μm), where p_i is the probability of each drop size class d_i for $Re_l = 1120$ measured at $x = 25d_g$ for two gas velocities without and with gas swirl.

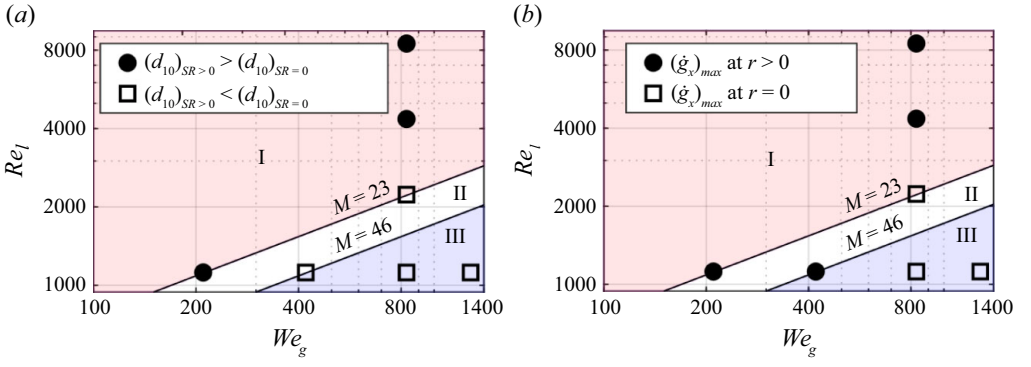

Figure 15. Regime map for separating swirling sprays based on (*a*) global drop size if swirl assists or hinders atomisation and (*b*) the radial profile if axial flux displays a maximum at the spray's centre or away from it.

The global p.d.f. shown in figure 11 can be categorised into two kinds. One is a p.d.f. with one mode, and the other is a p.d.f. with two modes. Such bimodal behaviour usually highlights the presence of two predominant mechanisms and is associated with high-M conditions here. Note that the axial flux corresponding to these conditions presents a maximum away from the centre. Therefore, the segregation of small droplets towards the centre due to high entrainment and centrifuging of the large droplets due to the high tangential velocity component towards the outer edge are believed to be the two mechanisms for such behaviour. Based on these understandings, two regime plots are shown in figure 15. Figure 15(*a*) separates the conditions that are assisted by swirl in making finer droplets from the conditions where swirl hinders spray formation, and figure 15(*b*) separates conditions when the axial flux is maximum away from the centreline from the conditions when axial flux is maximum at the centreline. It is apparent that M solely cannot define these boundaries appropriately. The following sums up the observations of figure 15.

(i) $M < 23$ (region I). In this region, swirl in the gas flow is responsible for producing bigger global drop size than the non-swirling condition. The axial flux in this region is strongly affected by swirl, leading to an off-centre maxima in the radial profile.
(ii) $M > 46$ (region III). In this region, swirl in the gas flow leads to reduction in the global drop size compared with the non-swirling conditions. The radial profiles of axial flux do not change shape on swirl addition.
(iii) $23 \leqslant M \leqslant 46$ (region II). In this region of intermediate M, the effect of swirl is less straightforward. Low values of the liquid Reynolds number yield off-centre

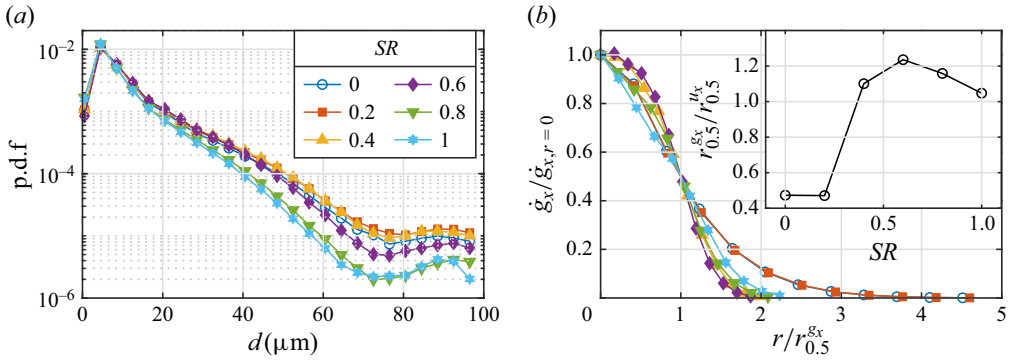

Figure 16. Global drop size distributions (a), and radial profiles of the axial flux (b) for different SR at $Re_l = 1120$ and $We_g = 830$ at $x = 25d_g$. The inset shows the ratio of the half-widths of the radial profiles of axial flux and longitudinal velocity, respectively.

maxima for the radial profiles of the axial flux, but can result in larger or smaller drop size depending on the Weber number. Off-centred maxima of flux profiles can be determined by $We_g < 400$ and larger drop size by $We_g < 200$ (note that these thresholds do not hold out of region II).

Although the discussion for a single swirling intensity ($SR = 0.8$) distinguishes the change in two prominent features of the spray, i.e. drop size and flux, compared with the non-swirling conditions, it stays short from informing on the dependence of these features on the swirl intensity. Therefore, gradual variations in SR values were attained for the $We_g = 830$, $Re_l = 1120$ case, found in region III of figure 15, to demonstrate these aspects and is presented in figure 16. The global drop size distributions shown in figure 16(a) are observed to have a similar bimodal distribution for all the swirling conditions as observed for figure 11(a). This result reaffirms the discussions on the influence of M in the determination of the shape of these distributions. In addition, the gradual decrease in the number of big drops with increasing swirl intensity when $SR > 0.4$ is apparent (probability densities in the $50 < d < 100$ μm range are decreased by 39 % and 75 % at $SR = 0.6$ and 0.8–1 compared with $SR \leqslant 0.4$). This effect leads to a generalised drop size reduction from the non-swirling condition. However, for $SR \leqslant 0.4$, the size is marginally bigger.

Figure 16(b) follows this up with a similar analysis of the radial profiles of axial flux for varying swirling intensities, presenting radial profiles of a common shape (centred maxima of the profiles with wider bell curve), that roughly collapse when normalised by the half-width radius $r_{0.5}^{g_x}$ (swirled cases display a slightly steeper shape than conditions with $SR \leqslant 0.2$). In addition, a drastic increase of $r_{0.5}^{g_x}$ (more than doubled when $SR \geqslant 0.4$, see inset) as the swirl effect becomes dominant is also observed, which is in line with the explanations given with a single swirling condition (figure 13). Clearly, when the effect of swirl is tangible, the flux profiles become wider than the velocity profiles (as $r_{0.5}^{g_x} > r_{0.5}$), displaying a similar shape. At the same time, the broadening of the flux radial profiles is estimated to be almost double for low-M conditions, with an off-centred maximum, emphasising the importance of the regime maps to relate liquid mass distributions in the spray. Note that Fong *et al.* (2024) also found that the radial profiles of axial flux change with SR but are not as much as the large changes reported here at low M, as they report profiles that are more or less flat in the vicinity of the centreline, then decay for larger radial distances (with a possible low-amplitude off-centred maximum). This complements the conclusions made in figures 13 and 16, with a possible continuum of shapes for the

radial profiles of axial flux in swirled spray as M increases. This analysis also leads to a profound understanding that swirl intensity alone, without any consideration for M values, imparts limited insight into the radial profile of droplet size and spatial variation of the mass flux. This also calls for further investigations on how the change of shape gradually occurs through variations of M for swirled spray and at varied swirl intensities. Therefore, this discussion adds immensely to the scarcely explored literature on swirling sprays.

In the present investigation, the characteristics of swirling sprays are compared with their non-swirling counterparts. We observed that the carrier phase velocity field is affected due to the introduction of swirl: (*a*) the decay rate of the axial velocity increases and consequently the spread of the jet also increases; (*b*) the radial velocity profile in the plane perpendicular to the axial plane is self-similar, with profiles collapsing when the radius is non-dimensionalised with $r_{0.5}$ and the velocity by its maxima. Interestingly, the axial slip of swirling sprays was observed to be negative, unlike the non-swirling sprays. The breakup mechanism is known to transition due primarily to the change in the gas Weber number We_g, so does the radial drop size profile. For the low-We_g conditions in non-swirling spray, i.e. when the flapping motion of the liquid jet plays a key role in breakup, the mean droplet size d_{10} radial profiles are '∪'-shaped. However, at high We_g, irrespective of the liquid Reynolds number Re_l, the non-swirling spray is '∼'-shaped, maximum at the centre, then only slightly decreasing then increasing again. However, for the swirling spray, this shape is observed to be '∪'-shaped, irrespective of We_g and Re_l, with the presence of inflection point. The curvature is especially high when the pressure ratio values are low. In such conditions, the maxima of the radial flux profile shifts away from the centre. However, low-M swirling conditions display a wider bell curve than the non-swirling spray. Based on this understanding, a regime map was established, showing the distinction between such cases, which clearly demonstrates the non-trivial nature of the dependence of spray dispersion on M values. In addition, the role of gas swirl in the assistance and hindrance of forming fine sprays at high- and low-M values, respectively, is represented through another regime map. Irrespective of the regimes identified for swirling conditions based on both the mentioned criteria, and also for the non-swirling conditions, a common observation is the positive radial gradient of drop size at the edge of spray. Therefore, an investigation to identify the characteristics of the droplets at the spray's edge for individual swirl value revealed that their linear response to the Eulerian time scales of the flow are observed to vary when the strength of the gas swirl increases. This investigation bears significance due to the increased requirement of swirling spray in different applications such as metal powder manufacturing.

Supplementary movies. Supplementary movies are available at https://doi.org/10.1017/jfm.2025.10924.

Funding. This research was funded, in whole or in part, by the Agence Nationale de la Recherche under grant number ANR-22-CE30-0003-01. A CC-BY 4.0 public copyright licence has been applied by the authors to the present document and will be applied to all subsequent versions up to the Author Accepted Manuscript arising from this submission, in accordance with the grant's open access conditions.

Declaration of interests. The authors report no conflict of interest.

References

Acharya, A.S., Deevi, S., Dhivyaraja, K., Tangirala, A.K. & Panchagnula, M.V. 2021 Spatio-temporal microstructure of sprays: data science-based analysis and modelling. *J. Fluid Mech.* **912**, A19.

Ade, S.S., Kirar, P.K., Chandrala, L.D. & Sahu, K.C. 2023 Droplet size distribution in a swirl airstream using in-line holography technique. *J. Fluid Mech.* **954**, A39.

Albrecht, H.-E., Borys, M., Damaschke, N., Tropea, C., Albrecht, H.-E., Borys, M., Damaschke, N. & Tropea, C. 2003 *Laser Doppler and Phase Doppler Measurement Techniques*. Springer.

ANGRIMAN, S., FERRAN, A., ZAPATA, F., COBELLI, P.J., OBLIGADO, M. & MININNI, P.D. 2022 Clustering in laboratory and numerical turbulent swirling flows. *J. Fluid Mech.* **948**, A30.

BALACHANDAR, S. & EATON, J.K. 2010 Turbulent dispersed multiphase flow. *Annu. Rev. Fluid Mech.* **42** (1), 111–133.

BEÉR, J.M. & CHIGIER, N.A. 1972 Combustion aerodynamics.

BILLANT, P., CHOMAZ, J.-M. & HUERRE, P. 1998 Experimental study of vortex breakdown in swirling jets. *J. Fluid Mech.* **376**, 183–219.

BRANDT, L. & COLETTI, F. 2022 Particle-laden turbulence: progress and perspectives. *Annu. Rev. Fluid Mech.* **54** (1), 159–189.

CHIGIER, N. & FARAGO, Z. 1992 Morphological classification of disintegration of round liquid jets in a coaxial air stream. *Atomiz. Spray.* **2** (2), 137–153.

CHUNG, J.N. & TROUTT, T.R. 1988 Simulation of particle dispersion in an axisymmetric jet. *J. Fluid Mech.* **186**, 199–222.

CROW, S.C. & CHAMPAGNE, F.H. 1971 Orderly structure in jet turbulence. *J. Fluid Mech.* **48** (3), 547–591.

DELON, A., CARTELLIER, A. & MATAS, J.-P. 2018 Flapping instability of a liquid jet. *Phys. Rev. Fluids* **3** (4), 043901.

DHIVYARAJA, K., GADDES, D., FREEMAN, E., TADIGADAPA, S. & PANCHAGNULA, M.V. 2019 Dynamical similarity and universality of drop size and velocity spectra in sprays. *J. Fluid Mech.* **860**, 510–543.

DIMOTAKIS, P.E., MIAKE-LYE, R.C. & PAPANTONIOU, D.A. 1983 Structure and dynamics of round turbulent jets. *Phys. Fluids* **26** (11), 3185–3192.

DUMOUCHEL, C. 2008 On the experimental investigation on primary atomization of liquid streams. *Exp. Fluids* **45**, 371–422.

DUNAND, A., CARREAU, J.-L. & ROGER, F. 2005 Liquid jet breakup and atomization by annular swirling gas jet. *Atomiz. Spray* **15** (2), 223–247.

EATON, J.K. & FESSLER, J.R. 1994 Preferential concentration of particles by turbulence. *Intl J. Multiphase Flow* **20**, 169–209.

FAVRE-MARINET, M., CAMANO, E.B. & SARBOCH, J. 1999 Near-field of coaxial jets with large density differences. *Exp. Fluids* **26** (1), 97–106.

FONG, K.O., XUE, X., OSUNA-OROZCO, R. & ALISEDA, A. 2024 Gas–liquid coaxial atomization with swirl in high-pressure environments. *Intl J. Multiphase Flow* **174**, 104767.

GOUNDER, J.D., KOURMATZIS, A. & MASRI, A.R. 2012 Turbulent piloted dilute spray flames: flow fields and droplet dynamics. *Combust. Flame* **159** (11), 3372–3397.

GÜRZING, S., THIEBES, A.L., CORNELISSEN, C.G., JOCKENHOEVEL, S. & REDDEMANN, M.A. 2022 Suitability of bronchoscopic spraying for fluid deposition in lower airway regions: fluorescence analysis on a transparent in vitro airway model. *J. Aerosol Med. Pulmon. Drug Delivery* **35** (5), 269–277.

HARDALUPAS, Y., TAYLOR, A.M.K.P. & WHITELAW, J.H. 1989 Velocity and particle-flux characteristics of turbulent particle-laden jets. *Proc. R. Soc. Lond. A. Math. Phys. Sci.* **426** (1870), 31–78.

HARDALUPAS, Y., TAYLOR, A.M.K.P. & WHITELAW, J.H. 1990 Velocity and size characteristics of liquid-fuelled flames stabilized by a swirl burner. *Proc. R. Soc. Lond. A. Math. Phys. Sci.* **428** (1874), 129–155.

HARDALUPAS, Y., TAYLOR, A.M.K.P. & WHITELAW, J.H. 1992 Particle dispersion in a vertical round sudden-expansion flow. *Philos. Trans. R. Soc. Lond. Ser. A: Phys. Engng Sci.* **341** (1662), 411–442.

HARDALUPAS, Y. & WHITELAW, J.H. 1994 Characteristics of sprays produced by coaxial airblast atomizers. *J. Propul. Power* **10** (4), 453–460.

HOFFMANN, S., LENZE, B. & EICKHOFF, H. 1997 *Results of Experiments and Models for Predicting Stability Limits of Turbulent Swirling Flames*, vol. 78699. American Society of Mechanical Engineers.

HOPFINGER, E.J. & LASHERAS, J.C. 1996 Explosive breakup of a liquid jet by a swirling coaxial gas jet. *Phys. Fluids* **8** (7), 1696–1698.

HUCK, P.D., OSUNA-OROZCO, R., MACHICOANE, N. & ALISEDA, A. 2022 Spray dispersion regimes following atomization in a turbulent co-axial gas jet. *J. Fluid Mech.* **932**, A36.

HUSSEIN, H.J., CAPP, S.P. & GEORGE, W.K. 1994 Velocity measurements in a high-Reynolds-number, momentum-conserving, axisymmetric, turbulent jet. *J. Fluid Mech.* **258**, 31–75.

JEROME, J., MARTY, S., MATAS, J.-P., ZALESKI, S. & HOEPFFNER, J. 2013 Vortices catapult droplets in atomization. *Phys. Fluids* **25** (11), 112109.

KACZMAREK, M., OSUNA-OROZCO, R., HUCK, P.D., ALISEDA, A. & MACHICOANE, N. 2022 Spatial characterization of the flapping instability of a laminar liquid jet fragmented by a swirled gas co-flow. *Intl J. Multiphase Flow* **152**, 104056.

KANDASAMY, R., HO, J.Y., LIU, P., WONG, T.N., TOH, K.C. & CHUA, S.J. 2022 Two-phase spray cooling for high ambient temperature data centers: Evaluation of system performance. *Appl. Energy* **305**, 117816.

KO, N.W.M. & DAVIES, P.O.A.L. 1971 The near field within the potential cone of subsonic cold jets. *J. Fluid Mech.* **50** (1), 49–78.

KUHLMAN, J.M. 1987 Variation of entrainment in annular jets. *AIAA J.* **25** (3), 373–379.
KUMAR, A. & SAHU, S. 2019 Large scale instabilities in coaxial air-water jets with annular air swirl. *Phys. Fluids* **31** (12), 124103.
KWARK, J.-H., JEONG, Y.-K., JEON, C.-H. & CHANG, Y.-J. 2005 Effect of swirl intensity on the flow and combustion of a turbulent non-premixed flat flame. *Flow, Turbul. Combust.* **73**, 231–257.
LALLART, A., CARTELLIER, A., GARNIER, P., CHARLAIX, E. & LORENCEAU, E. 2024 The fluid mechanics of spray cleaning: when the stress amplification at the contact lines of impacting droplets nano-scraps particles. *J. Fluid Mech.* **1000**, A31.
LASHERAS, J.C., VILLERMAUX, E. & HOPFINGER, E.J. 1998 Break-up and atomization of a round water jet by a high-speed annular air jet. *J. Fluid Mech.* **357**, 351–379.
LASHERAS, J.C. & HOPFINGER, E.J. 2000 Liquid jet instability and atomization in a coaxial gas stream. *Annu. Rev. Fluid Mech.* **32** (1), 275–308.
LAU, T.C.W. & NATHAN, G.J. 2014 Influence of Stokes number on the velocity and concentration distributions in particle-laden jets. *J. Fluid Mech.* **757**, 432–457.
LAU, T.C.W. & NATHAN, G.J. 2016 The effect of Stokes number on particle velocity and concentration distributions in a well-characterised, turbulent, co-flowing two-phase jet. *J. Fluid Mech.* **809**, 72–110.
LAZARO, B.J. & LASHERAS, J.C. 1992 Particle dispersion in the developing free shear layer. Part 2. Forced flow. *J. Fluid Mech.* **235**, 179–221.
LIEPMANN, D. & GHARIB, M. The role of streamwise vorticity in the near-field entrainment of round jets. *J. Fluid Mech.* **245**, 643–668.
LING, Y., FUSTER, D., TRYGGVASON, G. & ZALESKI, S. 2019 A two-phase mixing layer between parallel gas and liquid streams: multiphase turbulence statistics and influence of interfacial instability. *J. Fluid Mech.* **859**, 268–307.
LONGMIRE, E.K. & EATON, J.K. 1992 Structure of a particle-laden round jet. *J. Fluid Mech.* **236**, 217–257.
LOZANO, A. & BARRERAS, F. 2001 Experimental study of the gas flow in an air-blasted liquid sheet. *Exp. Fluids* **31** (4), 367–376.
MACHICOANE, N., RICARD, G., OSUNA-OROZCO, R., HUCK, P.D. & ALISEDA, A. 2020 Influence of steady and oscillating swirl on the near-field spray characteristics in a two-fluid coaxial atomizer. *Intl J. Multiphase Flow* **129**, 103318.
MAKHNENKO, I., ALONZI, E.R., FREDERICKS, S.A., COLBY, C.M. & DUTCHER, C.S. 2021 A review of liquid sheet breakup: perspectives from agricultural sprays. *J. Aerosol Sci.* **157**, 105805.
MANISH, M. & SAHU, S. 2019 Droplet clustering and local spray unsteadiness in air-assisted sprays. *Exp. Therm. Fluid Sci.* **100**, 89–103.
MARMOTTANT, P. & VILLERMAUX, E. 2004 On spray formation. *J. Fluid Mech.* **498**, 73–111.
MATAS, J.-P., DELON, A. & CARTELLIER, A. 2018 Shear instability of an axisymmetric air–water coaxial jet. *J. Fluid Mech.* **843**, 575–600.
MODARRESS, D., TAN, H. & ELGHOBASHI, S. 1984 Two-component LDA measurement in a two-phase turbulent jet. *AIAA J.* **22** (5), 624–630.
MULIADI, A. & SOJKA, P.E. 2010 A review of pharmaceutical tablet spray coating. *Atomiz. Sprays* **20** (7), 611–638.
OBERLEITHNER, K., SIEBER, M., NAYERI, C.N., PASCHEREIT, C.O., PETZ, C., HEGE, H.-C., NOACK, B.R. & WYGNANSKI, I. 2011 Three-dimensional coherent structures in a swirling jet undergoing vortex breakdown: stability analysis and empirical mode construction. *J. Fluid Mech.* **679**, 383–414.
OSUNA OROZCO, R. 2021 Characterization and control of electrostatically assisted two-fluid coaxial atomization. PhD thesis.
OSUNA-OROZCO, R., MACHICOANE, N., HUCK, P.D. & ALISEDA, A. 2019 Feedback control of coaxial atomization based on the spray liquid distribution. *Atomiz. Sprays* **29** (6), 545–551.
OSUNA-OROZCO, R., MACHICOANE, N., HUCK, P.D. & ALISEDA, A. 2020 Feedback control of the spray liquid distribution of electrostatically assisted coaxial atomization. *Atomiz. Sprays* **30** (1), 1–9.
OSUNA-OROZCO, R., MACHICOANE, N., HUCK, P.D. & ALISEDA, A. 2022 Effect of electrostatic forcing on coaxial two-fluid atomization. *Phys. Rev. Fluids* **7** (7), 074301.
PANCHAPAKESAN, N.R. & LUMLEY, J.L. 1993 Turbulence measurements in axisymmetric jets of air and helium. Part 1. Air jet. *J. Fluid Mech.* **246**, 197–223.
PARK, C.J. & CHEN, L.-D. 1989 Experimental investigation of confined turbulent jets. Part 11: Particle-laden flow data. *AIAA J.* **27** (11), 1511–1516.
POPE, S.B. 2001 Turbulent flows. *Meas. Sci. Technol.* **12** (11), 2020–2021.
PRÉAUX, G., LASHERAS, J.C. & HOPFINGER, E.J. 1998 Atomization of a liquid jet by a high momentum coaxial swirling gas jet. In *Proc. 3rd Int. Conf. Multiphase Flow*.

PREVOST, F., BOREE, J., NUGLISCH, H.J. & CHARNAY, G. 1996 Measurements of fluid/particle correlated motion in the far field of an axisymmetric jet. *Intl J. Multiphase Flow* **22** (4), 685–701.

QADDAH, B., CHAPELLE, P., BELLOT, J.P., JOURDAN, J., KEWALRAMANI, G., DEBORDE, A., HAMMES, R. & RIMBERT, N. 2024 Primary and secondary breakup of molten Ti64 in an EIGA atomizer for metal powder production. *Powder Technol.* **438**, 119665.

RAJAMANICKAM, K. & BASU, S. 2017 Insights into the dynamics of spray–swirl interactions. *J. Fluid Mech.* **810**, 82–126.

RAJAMANICKAM, K. & BASU, S. 2018 Insights into the dynamics of conical breakdown modes in coaxial swirling flow field. *J. Fluid Mech.* **853**, 72–110.

REHAB, H., VILLERMAUX, E. & HOPFINGER, E.J. 1997 Flow regimes of large-velocity-ratio coaxial jets. *J. Fluid Mech.* **345**, 357–381.

ROSTAMI, A., LI, R. & KHEIRKHAH, S. 2024 Three-dimensional clustering characteristics of large-Stokes-number dilute sprays interacting with turbulent swirling co-flows. *J. Fluid Mech.* **999**, A73.

ROSTAMI, A., LI, R. & KHEIRKHAH, S. 2025 Three-dimensional positioning, sizing, and velocimetry of dilute sprays using paired astigmatic interferometric particle imaging (PAIPI). *Exp. Fluids* **66** (6), 124.

SAHU, S. *et al.* 2018 Analysis of droplet clustering in air-assist sprays using voronoi tessellations. *Phys. Fluids* **30** (12), 123305.

SBRIZZAI, F., VERZICCO, R., PIDRIA, M.F. & SOLDATI, A. 2004 Mechanisms for selective radial dispersion of microparticles in the transitional region of a confined turbulent round jet. *Intl J. Multiphase Flow* **30** (11), 1389–1417.

SHUEN, J.-S., SOLOMON, A.S.P., ZHANG, Q.F. & FAETH, G.M. 1985 Structure of particle-laden jets - measurements and predictions. *AIAA J.* **23** (3), 396–404.

SINGH, G., JUDDOO, M., KOURMATZIS, A., DUNN, M.J. & MASRI, A.R. 2020 Heat release zones in turbulent, moderately dense spray flames of ethanol and biodiesel. *Combust. Flame* **220**, 298–311.

SQUIRES, K.D. & EATON, J.K. 1990 Particle response and turbulence modification in isotropic turbulence. *Phys. Fluids A: Fluid Dyn.* **2** (7), 1191–1203.

TAKAHASHI, M., FUKUI, R., TSUJIMOTO, K., ANDO, T. & SHAKOUCHI, T. 2023 Helical structures in a temporally developing round jet in the developed state. *Flow Turbul. Combust.* **111** (1), 59–79.

TOLFTS, O., DEPLUS, G. & MACHICOANE, N. 2023 Statistics and dynamics of a liquid jet under fragmentation by a gas jet. *Phys. Rev. Fluids* **8** (4), 044304.

TOLFTS, O., RACK, A. & MACHICOANE, N. 2024 Morphology and dynamics of the liquid jet in high-speed gas-assisted atomization retrieved through synchrotron-based high-speed X-ray imaging. *Intl J. Multiphase Flow* **181**, 105004.

TRATNIG, A. & BRENN, G. 2010 Drop size spectra in sprays from pressure-swirl atomizers. *Intl J. Multiphase Flow* **36** (5), 349–363.

TSO, J. & HUSSAIN, F. Organized motions in a fully developed turbulent axisymmetric jet. *J. Fluid Mech.* **203**, 425–448.

ÜNAL, A. 1989 Liquid break-up in gas atomization of fine aluminum powders. *Metall. Trans. B* **20**, 61–69.

WU, H., ZHANG, F., ZHANG, Z. & HOU, L. 2022 Atomization and droplet dynamics of a gas–liquid two-phase jet under different mass loading ratios. *Intl J. Multiphase Flow* **151**, 104043.

YARIN, A.L., ROISMAN, I.V. & TROPEA, C. 2017 *Collision Phenomena in Liquids and Solids*. Cambridge University Press.

YODA, M., HESSELINK, L. & MUNGAL, M.G. 1992 The evolution and nature of large-scale structures in the turbulent jet. *Phys. Fluids A: Fluid Dyn.* **4** (4), 803–811.

ZANDIAN, A., SIRIGNANO, W.A. & HUSSAIN, F. 2018 Understanding liquid-jet atomization cascades via vortex dynamics. *J. Fluid Mech.* **843**, 293–354.

ZHOU, H., HAWKES, E.R., LAU, T.C.W., CHIN, R., NATHAN, G.J. & WANG, H. 2022 Understanding of turbulence modulation and particle response in a particle-laden jet from direct numerical simulations. *J. Fluid Mech.* **950**, A3.